J. Fluid Mech. (1990), *vol.* 216, *pp.* 1–34
Printed in Great Britain

Quantitative three-dimensional imaging and the structure of passive scalar fields in fully turbulent flows

By RAHUL R. PRASAD AND K. R. SREENIVASAN
Mason Laboratory, Yale University, New Haven, CT 06520, USA

(Received 3 June 1989)

The three-dimensional turbulent field of a passive scalar has been mapped quantitatively by obtaining, effectively instantaneously, several closely spaced parallel two-dimensional images; the two-dimensional images themselves have been obtained by laser-induced fluorescence. Turbulent jets and wakes at moderate Reynolds numbers are used as examples. The working fluid is water. The spatial resolution of the measurements is about four Kolmogorov scales. The first contribution of this work concerns the three-dimensional nature of the boundary of the scalar-marked regions (the 'scalar interface'). It is concluded that interface regions detached from the main body are exceptional occurrences (if at all), and that in spite of the large structure, the randomness associated with small-scale convolutions of the interface are strong enough that any two intersections of it by parallel planes are essentially uncorrelated even if the separation distances are no more than a few Kolmogorov scales. The fractal dimension of the interface is determined directly by box-counting in three dimensions, and the value of 2.35 ± 0.04 is shown to be in good agreement with that previously inferred from two-dimensional sections. This justifies the use of the method of intersections. The second contribution involves the joint statistics of the scalar field and the quantity χ^* (or its components), χ^* being the appropriate approximation to the scalar 'dissipation' field in the inertial–convective range of scales. The third aspect relates to the *multifractal scaling properties* of the spatial intermittency of χ^*; since all three components of χ^* have been obtained effectively simultaneously, inferences concerning the scaling properties of the individual components and their sum have been possible. The usefulness of the multifractal approach for describing highly intermittent distributions of χ^* and its components is explored by measuring the so-called singularity spectrum (or the $f(\alpha)$-curve) which quantifies the spatial distribution of various strengths of χ^*. Also obtained is a time sequence of two-dimensional images with the temporal resolution on the order of a few Batchelor timescales; this enables us to infer features of temporal intermittency in turbulent flows, and qualitatively the propagation speeds of the scalar interface. Finally, a few issues relating to the resolution effects have been addressed briefly by making point measurements with the spatial and temporal resolutions comparable with the Batchelor lengthscale and the corresponding timescale.

1. Introduction

A capability to map quantitatively the turbulent velocity and/or passive scalar fields in three-dimensional space would be of immense value in understanding the dynamics as well as the topology of spatial structures. The issues that can be settled

by such efforts are both basic and practical, and we assume that it is not necessary to dwell on them at great length. Some examples are the three-dimensional nature of the interface bounding the vortical or scalar-marked regions, the joint statistics of the scalar concentration and its dissipation rate (of interest in fast chemistry reactions), the scaling relations of energy and scalar dissipation fields, issues concerning local isotropy, shapes and sizes of coherent structures, etc. Here, we describe a technique for mapping quantitatively the three-dimensional field of a passive scalar, and present results concerning several aspects associated with it. We also obtain with excellent resolution a temporal sequence of the scalar field both in one and two dimensions.

The technique consists of obtaining several closely spaced parallel two-dimensional images essentially instantaneously, and reconstructing the three-dimensional field on the computer using appropriate reconstruction algorithms. Two-dimensional images are obtained by the laser-induced fluorescence (LIF) technique (see, for example, Dimotakis, Lye & Papantoniou 1983). LIF involves doping the turbulent flow of interest by a fluorescent dye, inducing fluorescence by illuminating it with a thin sheet of laser light, and capturing the fluorescence radiation in the plane on to a digital camera. Under conditions to be discussed later, the fluorescence radiation is directly proportional to the dye concentration. Several such two-dimensional images of the concentration field are obtained in rapid succession by sweeping the laser sheet through the flow field. The succession of two-dimensional images is captured *quantitatively* on an array of charge-coupled devices (CCD) using a framing camera capable of operating at the rate of 10^4 frames per second. The time lapse during the entire sequence is small enough that effectively no fluid motion occurs even on the smallest dynamical scale. The digital data are then processed on a computer.

In the past, single 'point' measurements of the three components of the scalar dissipation have been made by using a combination of cold wires (e.g. Sreenivasan, Antonia & Danh 1977). In recent years, several research groups (Yip, Fourguette & Long 1986; Kychakoff *et al.* 1987; Agüí & Hesselink 1988) have taken advantage of the repeatability of the large structure in externally driven flows, and have obtained the scalar field in three dimensions. So far as we are aware, the only previous successful effort similar in scope to the present (namely the quantitative mapping of the passive scalar field in naturally developing turbulent flows) is due to Yip *et al.* (1987); see also Yip (1988). Yip *et al.* essentially developed the present technique and used it in gas jets. We use LIF instead of Rayleigh scattering and work with moderate-Reynolds-number water jets. It is unfortunate that with Yip's measurements there were difficulties in matching pixel positions in nearby parallel images, which made it difficult to extract quantitative information concerning the derivatives of the scalar field. In the present measurements, this difficulty has been surmounted as described in §2.4.

Two other efforts at three-dimensional imaging must be mentioned. A closely related effort by Lynch *et al.* (1985) in the near-wall region of low-Reynolds-number boundary layers appeared promising, but does not seem to have been pursued to a stage of fruition. Dahm & Buch (1989) used a stationary laser sheet and obtain successive frames at the same physical station at closely spaced times. This can be interpreted as three-dimensional imaging if Taylor's hypothesis is invoked in two dimensions; this hypothesis introduces uncertainties of unknown nature and may limit the effectiveness of the technique for certain purposes.

The present measurements have been made in round jets and wakes behind

circular cylinders, both generated at moderately large Reynolds numbers; the working fluid is water. A quantity of interest is the three-dimensional nature of the boundary marking the scalar-marked regions. Another quantity concerns (an approximation to) the dissipation field of the scalar concentration. Historically, such flow properties have been measured using point probes. When the Schmidt number Sc is unity or smaller (the Schmidt number being the ratio of the kinematic viscosity to the mass diffusivity of the scalar), the temporal characteristics of these measurements is excellent (good resolution, large record lengths) but the spatial information they yield is very limited. Two-dimensional LIF images in the recent past have provided useful information in a plane (e.g. Dimotakis *et al.* 1983; Prasad, Meneveau & Sreenivasan 1988). By the technique used here, on the other hand, we obtain information in three-dimensional space.

The best spatial resolution attained in the present experiments is about 3η, where the Kolmogorov scale η represents the smallest dynamically relevant scale (averaged over the flow domain). For passive scalars with $Sc \gg 1$, the appropriate smallest scale is the Batchelor scale $\eta_b = \eta Sc^{-\frac{1}{2}}$ (Batchelor 1959). The fluorescing dye (sodium fluorescein) has a Schmidt number of about 1900 (see Ware *et al.* 1983), and so the Batchelor scale is much smaller than the best resolution attained here. The essential point is that, in spite of this limitation, the present measurements will enable us to assess the *scaling properties* of the scalar dissipation structure in the inertial–convective range. In any case, we shall address the issues related to the resolution effects by two complementary sets of measurements. First, we obtain a time sequence of two-dimensional digital images with much finer temporal resolution. Incidentally, this permits us to make some remarks on temporal intermittency – an aspect that has not been studied before. Secondly, we obtain point measurements with spatial and temporal resolutions comparable with the Batchelor lengthscale and the corresponding timescale. Our remarks on these latter measurements will, however, be mainly limited to the issue of resolution. (A partial account of these measurements has appeared in Sreenivasan & Prasad 1989, and we expect to publish full details separately.)

The present measurements enable us to make qualitative statements about aspects such as the connectivity in three dimensions of the scalar-marked regions or the contiguity or otherwise of the interface. (We must make the obvious cautionary note that the scalar-marked regions do not necessarily correspond to regions containing turbulent vorticity.) We can also obtain the fractal dimension of the interface directly by box counting in three dimensions without invoking the additive laws (see Sreenivasan & Meneveau 1986; Prasad & Sreenivasan 1990) that one should use to interpret measurements in lower-dimensional subspaces.

We have computed low-order moments of the concentration field and of its 'dissipation' rate averaged over the spatial domain – the quotation marks here serving as a reminder that all scales have not been resolved. We explore in particular differences and similarities among the three components of the 'dissipation' field. Finally, joint statistics are obtained of the concentration fluctuation and its gradients, and the fluctuation and its 'dissipation'.

By experimental techniques such as the present, or by direct numerical solution on a massive computer of the governing equations, it is now possible to generate massive amounts of data. One of the pertinent questions today is to sort the data in a useful way. We have already addressed this issue partially in the context of two-dimensional images, for which we obtained the so-called generalized dimensions and

the singularity spectra. The significance of these quantities, without going into too many details here, is the following. In statistical mechanics, first-order information is carried by the thermodynamic quantities such as temperature, internal energy, entropy, free energy, etc. If we treat a given turbulent field as a statistical mechanical system (in the sense to be explained in §4), the generalized dimensions and the singularity spectra correspond to such 'thermodynamic' quantities. We extract these 'thermodynamic' quantities from the present data.

Section 2 contains a description of experimental techniques, while §3 is a summary of results related to the scalar interface and outer intermittency. In §4, the multifractal nature of the scalar 'dissipation' field (an example of 'internal intermittency') is described. The paper concludes with a discussion in §5 of the principal contributions of this work.

2. Flow facilities and experimental techniques

2.1. *Flow facilities*

Two fully developed turbulent flows were studied. The wake behind a circular cylinder was produced by lowering a tank of water (total mass about 800 kg) past a rigidly mounted cylinder. The cylinder used was 1 cm in diameter and had an aspect ratio of 58. The tank was lowered at a constant speed of 15 cm/s by means of a hydraulic lift. The reason that the tank, rather than the cylinder, was moved is that the water-filled tank, being much more massive than the cylinder, vibrates far less; it also eliminates the need for elaborate flow management devices upstream of the flow generator. The fluorescent dye (sodium fluorescein) that seeped into the wake from a narrow channel cut along the length of the cylinder – either at the front or the back stagnation regions – was mixed by the turbulence in the wake. These dye-marked regions were imaged and analysed.

The Reynolds number of 1500 (based on the cylinder diameter and the free-stream relative speed) is moderate. The smallest dynamical scale, the Kolmogorov scale η, was estimated to be about 150 μm. The Batchelor scale $\eta_b = \eta Sc^{-\frac{1}{2}}$ was estimated to be of the order of 4 μm.

The axisymmetric jet was produced by allowing water to flow from a settling chamber through a nozzle of circular cross-section into a tank of still water at a constant speed of about 35 cm/s. The nozzle (diameter 1.2 cm) was contoured according a fifth-order polynomial to have zero slopes and curvature at the entrance and the exit. The contraction ratio was about 10. It was established by running separate air experiments that there were no internal separation in the nozzle. The water that issued from the nozzle was dyed with the fluorescent dye. Again, the flow regions marked by the dye were imaged. The Reynolds number based on nozzle diameter and velocity is about 4000, and the estimated Kolmogorov and Batchelor scales are 160 and 4 μm respectively.

2.2. *Mapping the flow field*

Since the basic experimental technique involves obtaining several parallel two-dimensional sections, details described in another paper (Prasad & Sreenivasan 1990) are relevant, and the reader is referred to it. Here, a brief summary of those aspects is provided. Additional details involved in three-dimensional imaging are described in full.

(*a*) *Two-dimensional imaging.* In both flows the dye concentration was mapped quantitatively using the LIF technique. Fluorescence was excited in the dye by

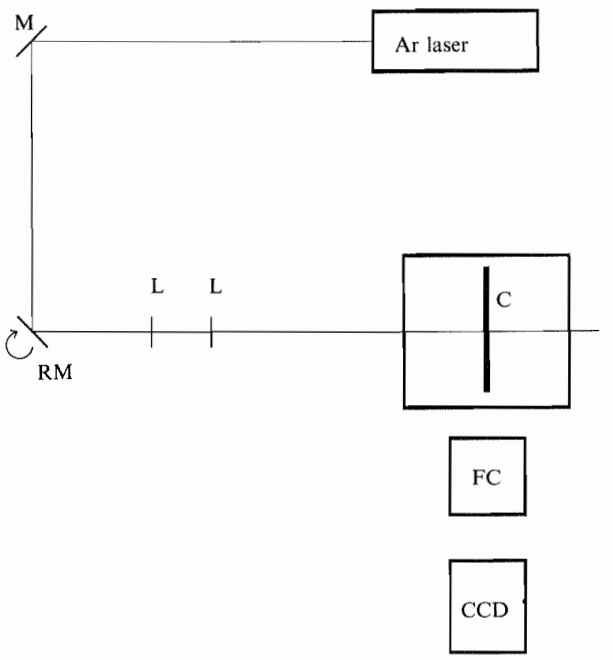

FIGURE 1. Schematic of the experimental apparatus used for three-dimensional imaging. Shown is the orientation of the cylinder whose wake is the object of imaging here. The continuous Argon laser has an output of 7 W.

illuminating the flow with a pulsed sheet of laser radiation. LIF occurs owing to the emission of photons when an excited ion or molecule decays back into its ground state. The lifetime of this process is on the order of 10^{-8} s. The number of photons emitted or the fluorescence intensity is proportional to the number of excited molecules or ions, which in turn is proportional to the number of ground-state ions or molecules and the illuminating light intensity. If the number of ground-state molecules is too large the fluorescence intensity decays as the light travels through the fluorescing medium; in such a case the fluorescence is saturated. If, however, the fluorescent dye concentration is small there is no significant change in the light intensity as the radiation traverses the medium. The fluorescence intensity is then directly proportional to the dye concentration. Care was taken to ensure that this was indeed the case in the present experiments. For instance, this was checked by doubling the dye concentration and observing that the intensity was correspondingly doubled.

(*b*) *Three-dimensional imaging.* If, instead of using a pulsed laser, a continuous sheet of laser radiation rapidly sweeping through the flow is used in conjunction with a camera having fast enough shutter speed and high enough repetition rate, several parallel instantaneous two-dimensional maps of the concentration field could be simultaneously obtained. If these planes are sufficiently close to each other one can reconstruct the three-dimensional field on a computer.

A schematic of the experimental apparatus is shown in figure 1. The beam from a 7 W Argon ion laser was guided to the flow field using the two mirrors labelled M and RM. The 4 mm diameter circular beam from the laser was converted to a sheet approximately 200 μm thick by a combination of two lenses L, one cylindrical (focal length = 25.4 mm) and another spherical (focal length = 1000 mm). The fluorescence

excited by the laser radiation was imaged by the framing camera FC, capable of acquiring a sequence of up to 16 frames at a rate of 10^4 frames/s. The images captured by the framing camera are then digitized and stored by the CCD camera having a large format CCD chip with an array of 1320×1035 pixels.

The flow seeded with the fluorescent dye was created in the tank; the figure shows the cylinder C used for the wake experiments. The sheet of laser radiation was swept through the flow field using the rotating mirror RM. At different discrete times, the sheet of light produces LIF in different planes. Given the framing rate of the camera, the speed of the rotating mirror was adjusted to yield an interplane distance of 500 μm. The distance of 140 cm between the rotating mirror and the region of the flow imaged is large compared to the interplane distance so that any two adjacent sheets of laser radiation can be regarded as parallel.

While in essence the scheme is simple, the technique is rendered possible only because of the speed at which the framing camera can acquire images. The exposure time for each image is 20 μs (which is negligibly small compared to all pertinent timescales in the flow) and the interframe period is 80 μs. Thus the overall time required to capture the sequence of 8 parallel two-dimensional images is 800 μs. This time is also tolerably small compared with the timescales of interest in the flow, enabling an effectively instantaneous measure to be obtained of the concentration field in three dimensions. The framing camera writes, in sequence, each of the images it acquires on a phosphor screen. This phosphor screen, which contains all the images acquired by the framing camera, is then imaged optically by the CCD camera. Thus a single frame of the CCD camera acquires all eight frames captured by the framing camera. This imposes a limitation on the spatial extent of each of the images. Also the resolution of the images is limited to the resolution of the phosphor screen, which was 7 line pairs per mm (i.e. the closest pair of lines that can be distinguished are 75 μm apart on the phosphor screen). Since the image reduction ratio used in the experiments is 6, this limits the spatial resolution to 450 μm. This is also the rationale for adjusting the speed of the rotating mirror to yield an interframe separation of about 500 μm.

A critical element of quantitative data analysis is the integrity of data. This is established here in two ways. First, several *a priori* considerations were given to enhance the quality of data acquisition. Second, comparisons were made as appropriate with previous data of known accuracy. Some of these data are obtained by standard point probes (such as cold wires in heated flows), but some of the present data have no analogues in such point measurements. In these latter cases, we have made comparisons with our own earlier data in which the entire CCD array was used to acquire single images. The resolution in the single frame images was better by a factor of three, and the flow extent imaged was larger by a factor of approximately four. Furthermore, since single frame measurements were made with a pulsed laser with a higher power density than the continuous laser used in the present experiments, the signal to noise ratio in the single frame measurements was substantially better; the quality of those signals has independently been established by several means including spectral analysis (Prasad & Sreenivasan 1990). Our estimate, based on a simple scheme described by Prasad & Sreenivasan (1989), is that this ratio in the single frame images was 65 whereas it was about half as high in the sequential images. For these reasons, we felt that a comparison with the earlier single frame measurements serves a useful purpose. To serve both as an example and for use at a later stage, we present in figure 2 a single frame image of a turbulent jet at a Reynolds number comparable with the present experiments.

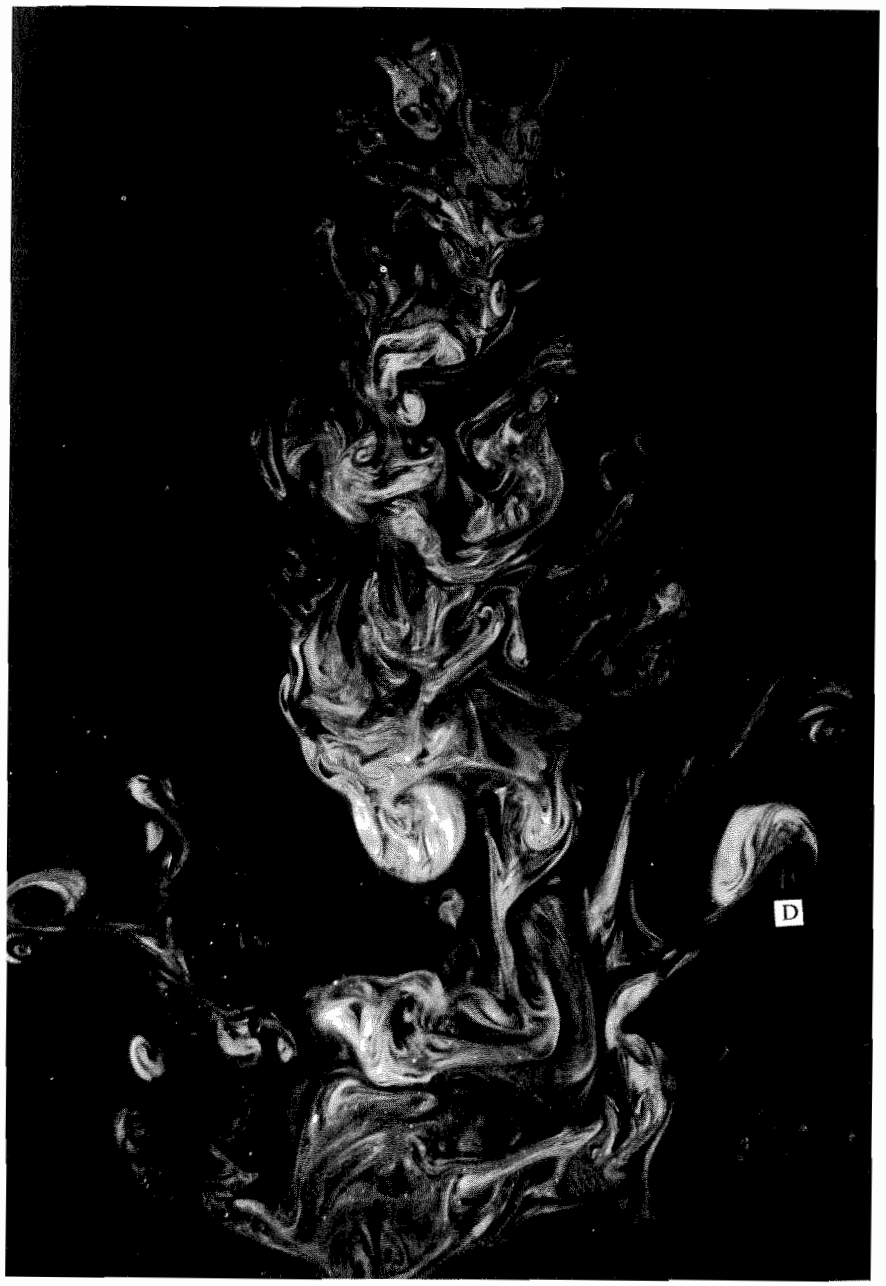

FIGURE 2. A two-dimensional slice of a turbulent jet at a nozzle Reynolds number of about 4000, obtained by the LIF technique. The entire extent of the CCD array (1300×1000 pixels was used to obtain this image. The region imaged extends from 8 to 24 diameters downstream of the nozzle. A Nd:YAG laser beam shaped into a sheet of about 250 μm thickness using a suitable lense was directed into the water tank into which the nozzle fluid containing small amounts of a fluorescing dye was emerging in the form of a jet. The laser had a power density of 2×10^7 J s^{-1} per pulse and a pulse duration of about 10 ns.

2.3. *Procedures for obtaining high quality images*

Below, we shall describe procedures essential for acquiring high quality images, but defer comparisons with single frame data to appropriate places in the later sections. The following remarks are specific to the jet, but similar remarks apply to other flows.

(i) If the jet is run for long periods of time the tank fluid gets contaminated by the dye and develops background fluorescence. To remove this source of noise it is necessary to acquire the image soon after the jet has settled down to its final state, and to flush out the tank water after each run and replace it with clear water.

(ii) For all data acquisition, the room was darkened to minimize spurious illumination. Water filtered by two filters in tandem was used. However, since filters do not remove all particles, the imaging system will detect, in addition to the fluorescence intensity from the nozzle fluid, the light scattered by stray particles present in the tank water. To separate scattered radiation from the fluorescence radiation, we note that the former has the same wavelength as that of the incoming laser light and that the fluorescence radiation is of a longer wavelength. Thus a long-pass optical filter was used to minimize the scattered radiation from the detector. Figure 3 ahows a comparison between the unfiltered and optically filtered spectra, obtained using a Jarrell–Ash monochrometer with 0.1 nm resolution. The sharp peak near 532 nm in figure 3(*a*) corresponds to the scattered laser radiation from stray particles. The fluorescence itself peaks at a slightly higher wavelength ($\sim$545 nm), but is essentially broadband. Hence, a filter which cuts off light below a wavelength of 540 nm would be desirable. A Corin optics long-pass filter with a cut off at 550 nm was used. The filter removes all but a small fraction of the 532 nm radiation, but also some of the fluorescence intensity (figure 3*b*). But this causes no problems if the incident laser intensity is sufficiently high (as in the present experiments).

(iii) The images were captured directly on the CCD camera digitally rather than first acquiring a photograph and subsequently digitizing it. This eliminates errors due to nonlinearities associated with the process of developing the photographic film, a process that cannot be controlled easily to the required accuracy. The dynamic range of the photographic film is also limited (roughly 300 grey levels) compared with that of a digitizing camera (4096 levels on the 12-bit camera used here).

(iv) The CCD array itself has a small amount of dark noise, i.e. the charge that accumulates on each pixel without any photon impingement. This dark noise was subtracted from the images.

(v) It is also necessary to take into account the variations in laser intensity across the sheet due to the laser itself, and the optics through which the beam passes. This was achieved by uniformly dyeing the fluid in a smaller tank and capturing the fluorescence intensity. (To ensure that the optical path was identical in the two cases, this smaller tank was placed in the middle of the big tank used in other experiments, filled with filtered water in the usual way. Needless to say, the jet was turned off.) This image was subsequently used to normalize all flow images. The corrected pixel intensity was calculated as:

$$\text{Corrected pixel intensity} = \frac{\text{(CCD intensity for the jet flow–noise)}}{\text{(CCD intensity for the uniformly dyed fluid–noise)}}. \tag{2.1}$$

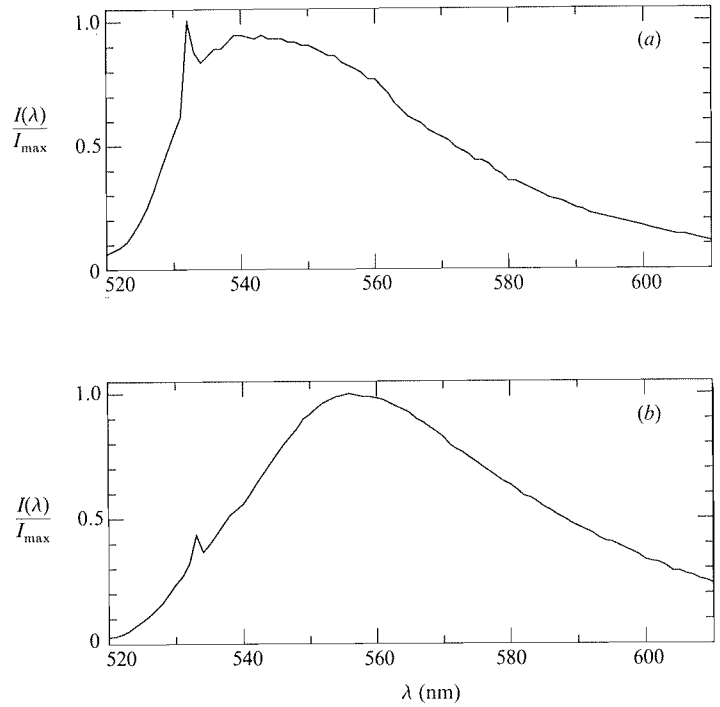

FIGURE 3. Comparison of the (*a*) unfiltered and (*b*) optically filtered fluorescence spectra. The sharp peak in (*a*) at a wavelength of 532 nm is the result of scattered radiation by particles in the fluid. By using an appropriate filter, its magnitude can be cut down significantly as seen in (*b*). The optical filter also cuts off some radiation due to fluorescence, but this is not a serious problem if the incident laser intensity is sufficiently large.

2.4. *Matching pixels in two successive parallel images*

We can thus obtain several parallel two-dimensional images. To obtain a composite three-dimensional image, it is necessary to make a perfect pixel match between two parallel images. This becomes especially important for obtaining concentration gradients in the z-direction, i.e. the direction in which the laser sheet rotates. To do this, a stationary object such as a meter scale or a stationary blob of dye in the plane of the visualization was imaged using the framing and CCD camera set-up. Each of the eight images of the sequence was first roughly cut and overlayed in pairs of two, taking the difference in intensity. The images were then moved around with respect to each other to minimize the difference in intensity. This minimum occurs only when the successive images have perfect pixel matching. No substantial distortion in shape of the stationary object was evident since the difference images were uniformly zero to excellent accuracy. Subsequent sequences of parallel planes were all aligned using this information; the difference in pixel intensity between two parallel planes gives a correct measure of the z-gradient of the concentration fluctuations.

2.5. *The experiments*

2.5.1. *The wake behind a circular cylinder*

As already remarked, each pixel has an area resolution of about 500 μm × 500 μm, and the distance between any two parallel images was arranged (by adjusting the speed of the rotating mirror) to be about 500 μm, so that quantitative data on the concentration field is available on a three-dimensional grid of 500 μm on the side. In

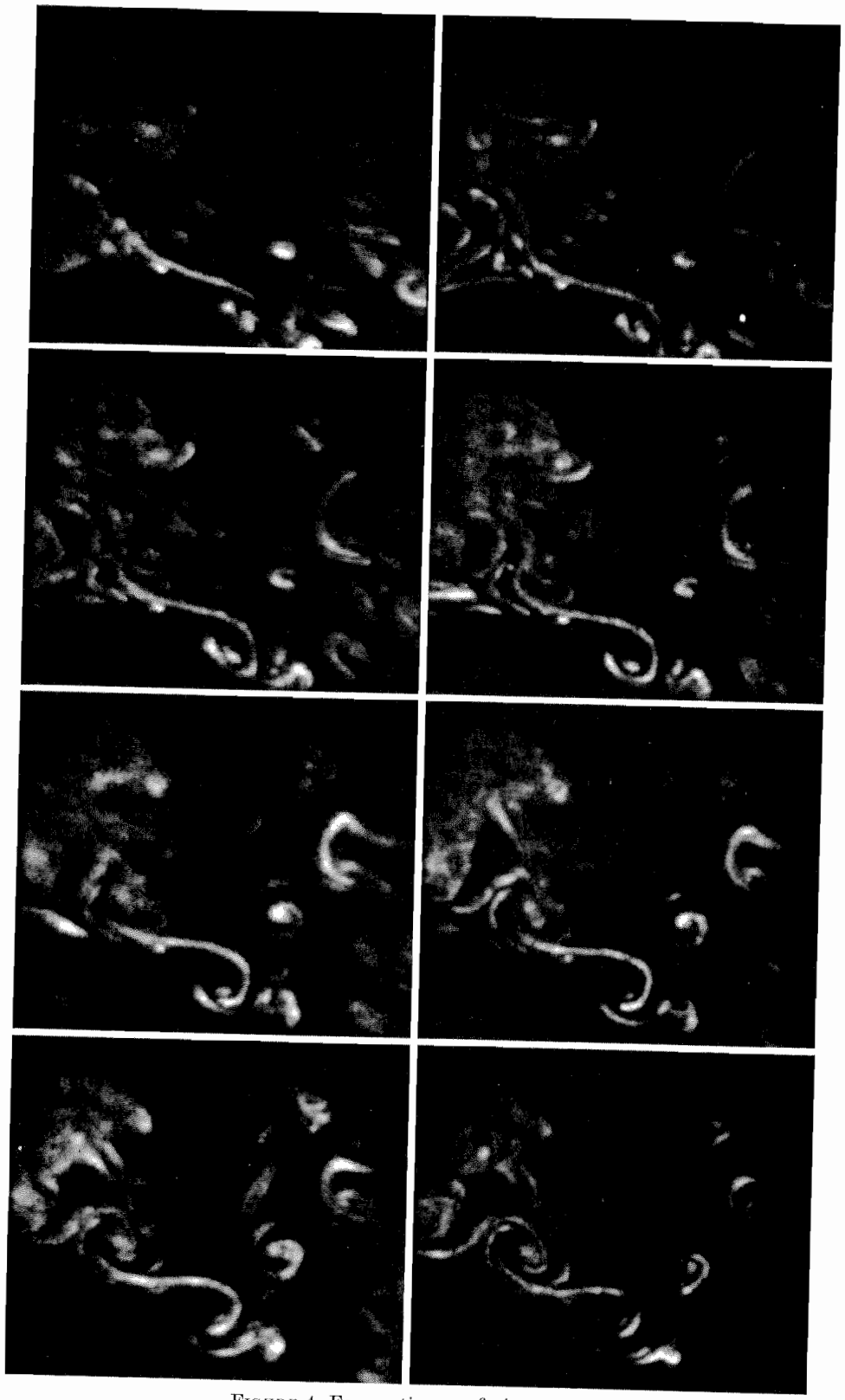

FIGURE 4. For caption see facing page.

dynamical terms, this resolution translates to about 4 Kolmogorov scales. So far, we have worked with eight parallel planes, each 175 pixels × 150 pixels in extent, although in rare instances double the number of parallel planes were obtained.

A typical experimental run proceeds as follows. The tank is filled with filtered water and raised using a hydraulic lift such that the circular cylinder is close to the bottom of the tank. After a long settling time, the dye is allowed to flow from the slit cut along the lower end of the cylinder and the tank is lowered at the desired speed producing the wake. As the tank drops the wake is illuminated by the rotating laser beam. When the bottom of the tank receeds to about 120 diameters downstream of the cylinder the shutters of the framing camera and the CCD camera are opened. A photodiode then detects the presence of the laser sheet in the region being imaged and triggers the electronics in the framing camera that acquires the images. Figure 4 shows the concentration field on a typical set of eight parallel planes. Each image of the wake extends approximately from 70 to 80 diameters downstream of the cylinder. The extent of the images in the direction of the largest shear is about 4 cylinder diameters on either side of the axis.

2.5.2. *The axisymmetric jet*

The procedure was essentially the same as that used for the wakes. The region imaged in the jet extended from 13 to 21 diameters downstream of the nozzle. The pixel resolution as well as the sheet thickness remain the same, and so quantitative data on the concentration field is available (as before) on a grid 500 μm on the side, with comparable resolution in terms of the Kolmogorov scale. Again eight parallel planes were acquired. The tank was first filled with clear, filtered water and the jet was turned on after considerable settling time. The flow was illuminated by the rotating laser sheet, and the image acquisition process was begun after the front of jet fluid emerging from the nozzle was well past the region that was imaged; this ensures that the images do not correspond to the transient states of the jet. The shutters on both framing and CCD cameras were opened and the imaging electronics on the framing camera triggered once the photodiode detected the laser sheet in the imaged volume. Figure 5 shows a typical set of eight parallel planes, each displaying the concentration of the scalar-marked regions.

3. The geometry of the scalar interface

An interface of primary interest in the study of turbulence is that separating regions of intense and zero vorticity; another such interface is that separating the scalar-marked regions of the flow from that remaining (the 'scalar interface'). From the images acquired here, one can examine several features of the scalar interface. Elsewhere (Prasad & Sreenivasan 1990) we have discussed several methods of marking this interface, but the simplest – and for the present purposes quite adequate – procedure involves setting an appropriate threshold on pixel intensity. Figure 6 shows the interface determined in each of the planes in a three-dimensional

FIGURE 4. Concentration field of scalar-marked regions of a turbulent wake behind a circular cylinder in a set of eight parallel planes. The flow moves from left to right in each of the eight planes. The plane farthest from the cameras is the plane in the bottom right corner of the image. As one moves from right to left in the figure and then from bottom to top the planes move closer to the cameras.

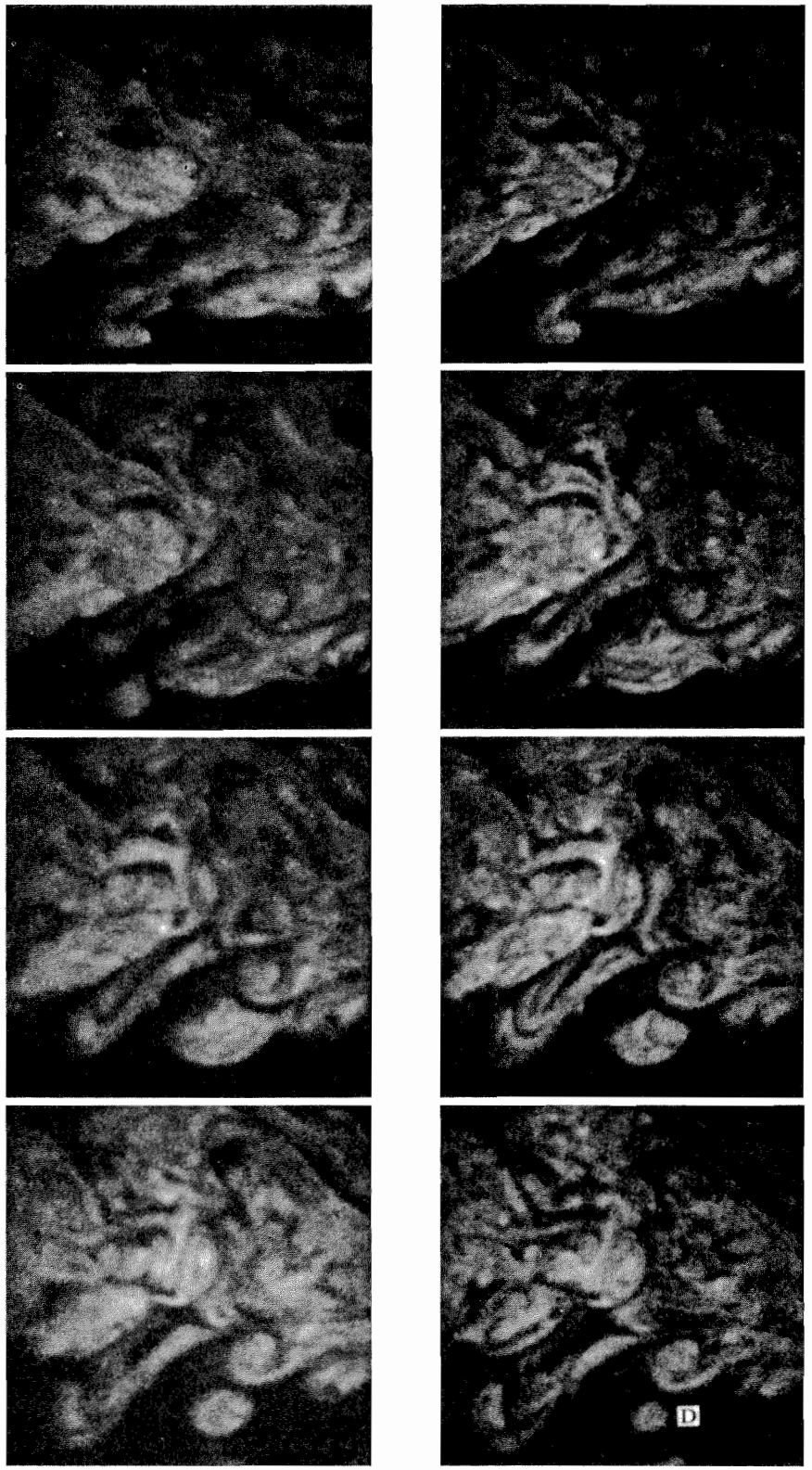

FIGURE 5. For caption see facing page.

sequence of wake images (marked in white). It is obvious that the interface is highly convoluted and three-dimensional. We now turn to its characterization.

3.1. *The intermittency factor*

An obvious manifestation of the interface, namely the intermittency factor, has been measured by many workers starting with Townsend (1948), Corrsin & Kistler (1955) and Klebanoff (1955). As defined originally, the intermittency factor defines the fraction of time that a point probe resides in the turbulent region as the turbulent structures convect past it. (Although the intermittency factor suffers from several drawbacks (Sreenivasan 1985; Chatwin & Sullivan 1989), we have chosen to present it mainly because of its historical status.) From two-dimensional images we can obtain a corresponding quantity by scanning several lines perpendicular to the jet axis and determining the number of pixels that are within the scalar-mixed region. For the fully turbulent regions of the jet, figure 7 shows a comparison of the intermittency factor from single frame images and from the present experiments. Except for some minor differences, which are probably due to the finite sample sizes, the agreement is good.

It must be mentioned that, in spite of figure 7, the peak intermittency factor is not always exactly unity for the concentration field of high-Schmidt-number scalars in the jet. We have noticed several occasions where the intermittency factor was clearly smaller than unity, although not very far from it. This appears to be different from the intermittency factor deduced from vorticity measurements (or its surrogates). Another difference is that the intermittency factor in most measurements of the latter variety is unity, or very close to it, until much further out in the radial direction than figure 7 shows. It is not clear how much of this is due to the relatively poor resolution of the single point probes in past measurements (typically several Kolmogorov thicknesses in the case of heated jets), and how much due to the high Schmidt number of the scalar in the present measurements. We know from temporal measurements in which the Batchelor scale has been resolved (to be described very briefly in §4.4) that resolution effects could be important in quantifying intermittency.

3.2. *Moments of the concentration field*

Table 1 compares the present data for jets on the skewness S and flatness factor F of the concentration field, c. These quantities are defined as

$$\left.\begin{aligned} S &= N^{-1}\sum (c-\langle c\rangle)^3/c'^3, \\ F &= N^{-1}\sum (c-\langle c\rangle)^4/c'^4, \end{aligned}\right\} \tag{3.1}$$

where $\langle c\rangle = N^{-1}\sum c$, and $c'^2 = N^{-1}\sum (c-\langle c\rangle)^2$, N being the total number of pixels in the image. Since no corresponding data exist except in our own earlier single frame images, we include in table 1 a comparison with only those data. The agreement for jets is good to within about 20%, and is similar for wakes.

For completeness, we present in figure 8 the probability density function (p.d.f.) of the concentration field. In the units of the abscissa, the dynamic range of the CCD array is 4096. (It would have been preferable, although not necessary for present purposes, to normalize the concentration by the nozzle fluid concentration;

FIGURE 5. Concentration field of scalar-marked regions of a turbulent axisymmetric jet in a set of eight parallel planes. The flow moves from left to right in each of the eight planes. The plane farthest from the cameras is the plane in the bottom right corner of the image. As one moves from right to left in the figure and then from bottom to top the planes move closer to the cameras.

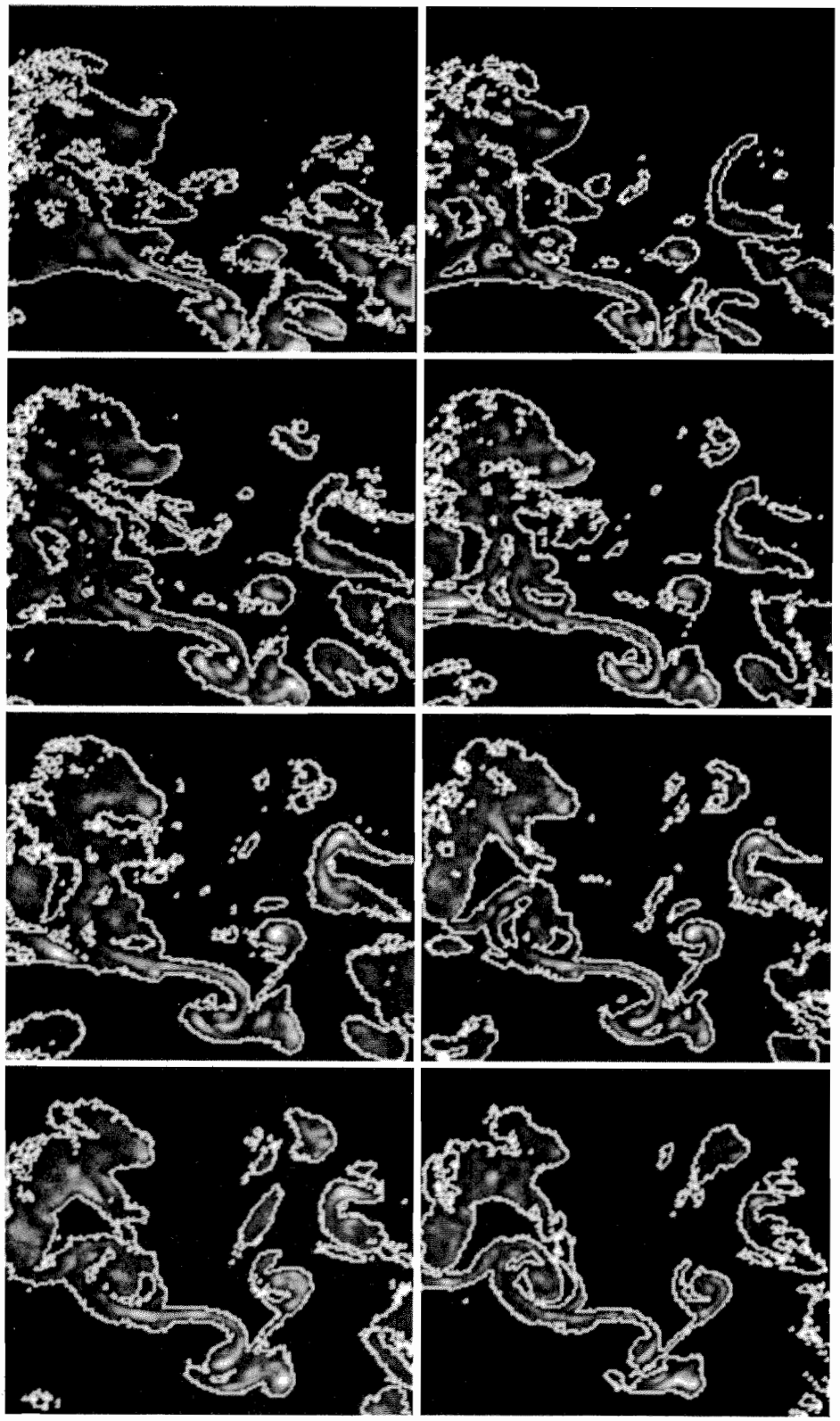

FIGURE 6. For caption see facing page.

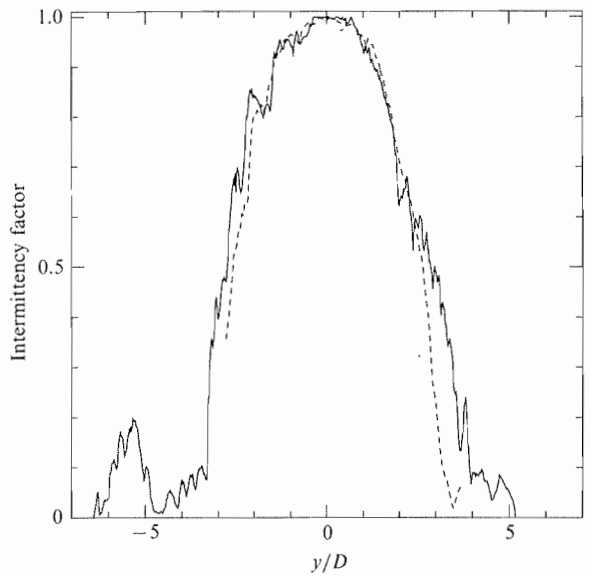

FIGURE 7. A comparison of the intermittency factor obtained from single frame images (——) as well as a three-dimensional sequence (– – – –). The averaging is performed over a streamwise extent of a few diameters. One single frame image and a complete set of eight images in the three-dimensional sequence were used.

	S	F
Present data (average of 9 images)	1.08	4.80
Data from single-frame images (average of 5 images)	1.31	4.52

TABLE 1. The skewness and flatness factor data of the concentration field from the three-dimensional sequence and from single-frame images

unfortunately, we do not know the latter quantity exactly.) The ordinate is simply the number of pixels with a given intensity normalized by the total number of pixels; to emphasize the tails, we have plotted the probability on the logarithmic scale. The peak in the low-concentration region corresponds to the external noise in the image. Following Bilger, Antonia & Sreenivasan (1978), this is related to the free-stream noise effects convolving with the concentration fluctuation in the flow; if the noise is small, it can be approximated reasonably well by a Gaussian. An interesting aspect of the plot is the exponential part over two decades of the probability scale. Similar exponential tails have been noticed in single point measurements in convection experiments at high Rayleigh numbers (Castaing *et al.* 1989).

3.3. *Three-dimensional structure of the scalar interface*

A two-dimensional image such as figure 2 shows some scalar-marked regions that appear to be detached from the main body of the flow; one such region is indicated by the letter D in figure 2. It is conceivable that this part is really not detached at

FIGURE 6. The sequence of wake images shown in figure 4 and the computer generated curve (shown in white) bounding the scalar-marked regions in the wake.

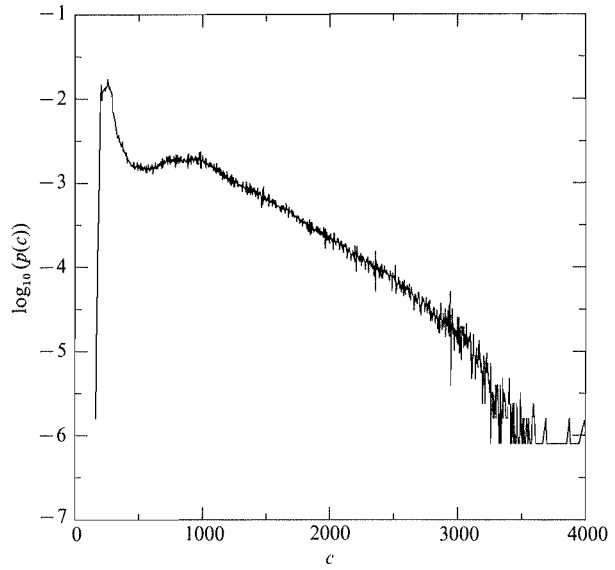

FIGURE 8. The probability density of the concentration field obtained from a typical set of images. The peak at the low concentration values is that due to free-stream noise effects. In the absence of noise, this will be a delta function corresponding to zero concentration.

all but is contiguous with the main body through an out-of-plane connection. This question can be resolved, at least partly, by the present sequence of parallel two-dimensional images. We have marked, again by the letter D, in the picture to the bottom right (farthest from the camera) of figure 5 to indicate an apparently detached region. However, the connection to the main jet is clearly established in the fourth picture in the sequence (second from the bottom in the left column). The wake images have similar occurrences also, but cases seem to exist where one may imagine isolated regions that appear and disappear within the sequence, leading to the potential conclusion that isolated patches indeed occur; our informed judgement from an examination of several sequences is that out-of-plane connections are plausible outside of the range of the images. But it appears safe to conclude that extensive disconnected regions do not exist. We draw attention to Pope (1988) which examines theoretically the conservation of the topology of material surfaces in incompressible flows and draws compatible conclusions.

A glance at the sequence of images in figures 4 and 5 shows that the large structure present in the interface persists from one parallel plane to the next. Their precise shapes and sizes cannot be ascertained without sophisticated signal processing, the most recent contribution in this regard being that of Everson, Sirovich & Sreenivasan (1990). The small structure is different from one picture to another. The small-scale variations are in fact so prevalent that *locally* any two neighbouring sections of the interface have very little correlation on the average. It is difficult to devise the most natural and intuitively appealing quantifier of this correlation that is also easy to compute, but a simple scheme may be based on the notion that the interface in one of its sections is locally well correlated with the neighbouring one if, for the same z-coordinate, the slopes in the (x, y)-plane are the same in the two sections. The following paragraph describes the implementation of this technique. We emphasize that this is not the only scheme possible.

All eight parallel planes forming a three-dimensional sequence are covered with

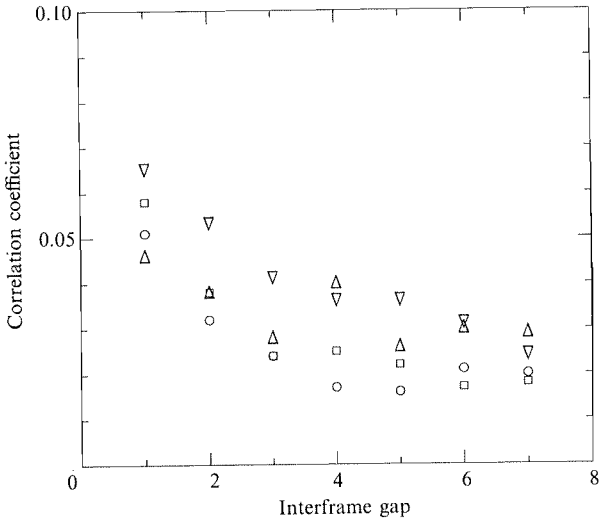

FIGURE 9. The cross-correlation coefficient between parallel sections of the interface separated by the interframe distance given on the abscissa. The closest interframe distance is on the order of 3η. The circle and rectangle symbols correspond to two sets of wakes, and the del and delta symbols to two sets of jets.

	Interface pixel position		Interface pixel position	Slope
IF	Upper left	AND	Lower right	−1
	Upper left		Lower left	−1
	Upper left		Upper right	0
	Lower left		Upper right	1
	Lower left		Lower right	0
	Lower right		Upper right	1

TABLE 2. The scheme used for assigning the slopes for the interface. See text for details

boxes, each of which is 2 pixels on the side. The direction of the image scanning (by arbitrary convention) is from left to right and top to bottom. If, in a given box, the top left pixel and the bottom right pixel are both interface pixels (that is, the interface passes through them), the slope of the interface for that box is considered negative and assigned the value −1. Other combinations of slopes and values assigned to them (1, −1 or 0) are listed in table 2. Once the slopes of the interface in all boxes containing the interface are assigned, the correlation calculation can be made. Consider any two parallel planes. If two boxes at the same location in the two planes have the same slope, the interface in the two boxes is obviously correlated, giving for the product of the slopes a value unity in those boxes. If the boxes have slopes 1 and −1 the interfaces in the two boxes are anti-correlated, and the index is assigned a value −1. Such comparisons are carried out for all pairs of boxes in the two chosen images, and a correlation is obtained by summing the indices. This sum is normalized to the total number of boxes containing the interface in one of the two planes. (The number of boxes in any two planes is not exactly the same, but the fractional difference is sufficiently small that the precise choice makes no substantial difference to the outcome.) The value 1 for the correlation coefficient defined in this way indicates perfect correlation, −1 indicates perfect anti-correlation and 0 indicates essentially uncorrelated images. Figure 9 shows the correlation coefficient

as a function of the interframe gap for two sets of image sequences in the jet and two sets in the wake. Even adjacent frames, separated by no more than about four Kolmogorov scales, are essentially uncorrelated; an increase in the interframe distance monotonically reduces this small correlation even further. Similar calculations can be made to quantify interface correlations at larger scales by considering boxes of size larger than those considered here. Because this operation amounts to a coarse graining, it is expected that the correlation increases with the box size.

3.4. *Fractal dimension results*

It has been shown that the interface is a fractal-like surface (Sreenivasan & Meneveau 1986); a quantity that characterizes a fractal being its fractal dimension, its measurement is of interest. The meaning of the fractal dimension and its usefulness in contexts of mixing and entrainment are discussed in Gouldin (1988) and Sreenivasan *et al.* (1989). We must remark, in view of the evidence (§3.3) that the interface is largely contiguous, that the fractal dimension is essentially a measure of the degree of its convolutedness (and not of fragmentation).

The determination of the fractal dimension of the interface (an object residing in the three-dimensional space in a complex way) by the direct procedure of covering them by boxes of varying sizes is most often not practicable. We have shown elsewhere (Sreenivasan & Meneveau 1986; Prasad & Sreenivasan 1990) that one way of measuring the fractal dimension of such surfaces is to measure the dimension D_s of the boundary of its intersection by a thin plane, and use the so-called law of additive codimensions (Marstrand 1954; Mandelbrot 1982); according to this law, the fractal dimension of the surface itself is given by D_s+1. The fractal dimension of such two-dimensional intersections has been measured and the results presented in Prasad & Sreenivasan (1990). It is important to examine whether such estimates agree with that measured from the full three-dimensional data. Equivalently, we want to assess directly the validity of the additive law; many indirect, but essentially complete, sets of arguments were presented in Prasad & Sreenivasan (1990).

In previous measurements from two-dimensional intersections, the box-counting algorithm was used to determine the fractal dimension. This algorithm (described, for example, in Sreenivasan & Meneveau 1986) basically requires that the plane of intersection (in which the boundary appears as a convoluted curve) be covered with disjoint square area elements ('boxes') of varying size. The number of boxes $N(r)$ required to cover the interface is then counted as a function of the size r of the box. If the curve is a fractal, an extended straight portion would be observed in log-log plots of $N(r)$ *vs.* r, the negative slope of the line being the fractal dimension D_s of the boundary in intersection. Figure 10 shows a typical log-log plot from an arbitrarily chosen image in the three-dimensional sequence for the wake; a reasonably well-defined straight line exits, and gives a D_s of 1.35 ± 0.05. Using the additive law, the dimension of the interface is 2.35 ± 0.05. This is in good agreement with the measured dimension of 2.36 from earlier single frame images. (Even though the resolution in the present images is only about a third as good as in our earlier single frame ones, we have shown elsewhere (Prasad 1989; Prasad & Sreenivasan 1990) that the difference in fractal dimensions obtained with resolutions of the order η and 4η is quite negligible.)

As already remarked, we cannot access the entire interface in three-dimensional space, its extent in the z-direction being limited to the range of approximately 4η to 32η. In this range, though, it is possible to use the direct method of covering the interface with three-dimensional boxes of varying sizes. The negative slope of the

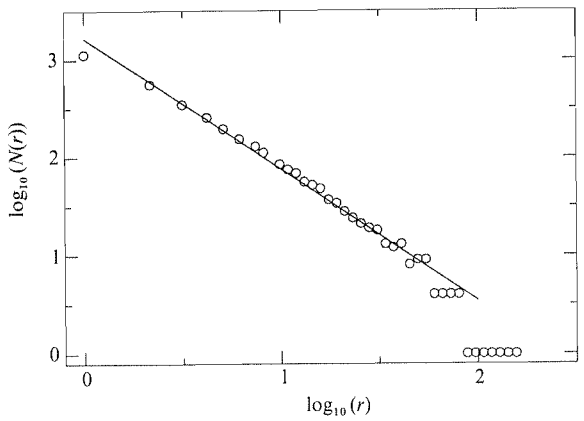

FIGURE 10. A typical log–log plot of the number $N(r)$ of square area elements ('boxes') of size r containing the interface *vs.* the box size r. The negative slope of the straight part gives the fractal dimension of the boundary in intersection ($=1.35$).

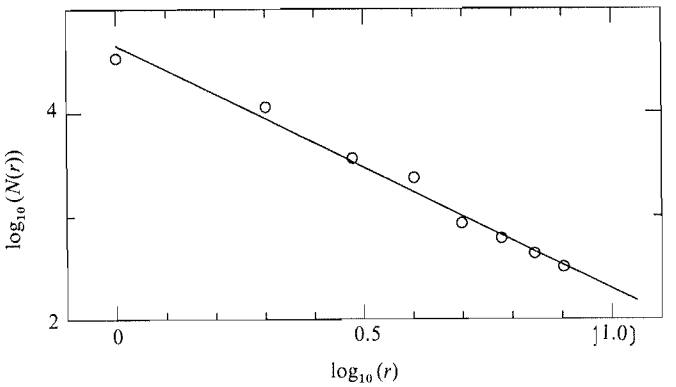

FIGURE 11. A typical log–log plot of the number of boxes $N(r)$ required to cover the accessible part of the interface in three-dimensional space *vs.* the size of the box r. Data from the axisymmetric turbulent jet. The dimension corresponding to the slope of the line drawn is about 2.35.

straight part of the log-log plots of $N(r)$ *vs.* r would directly yield the fractal dimension of the surface. Figure 11 shows a typical log-log plot for jets obtained by boxing the accessible portion of the surface; data for wakes shows identical behaviour. The scaling for both jets and wakes extends over the entire range available; the average fractal dimension is 2.35 ± 0.04 for both flows. This agrees rather well with earlier measurements from two-dimensional sections (Sreenivasan & Meneveau 1986; Prasad & Sreenivasan 1990), and the present results of figure 10. In our view, this establishes the fractal nature of the scalar interface in turbulent flows, and directly verifies the applicability of the method of intersections.

3.5. *A temporal sequence of images*

It is also possible using the procedure described above to acquire a temporal sequence of images. This is done by eliminating the rotating mirror in figure 1 and acquiring a set of images as before. The sequence of eight planes is now at the same physical location but traces the temporal evolution of the scalar-marked regions. Since the framing camera acquires images at 10^4 frames per second, the time delay between

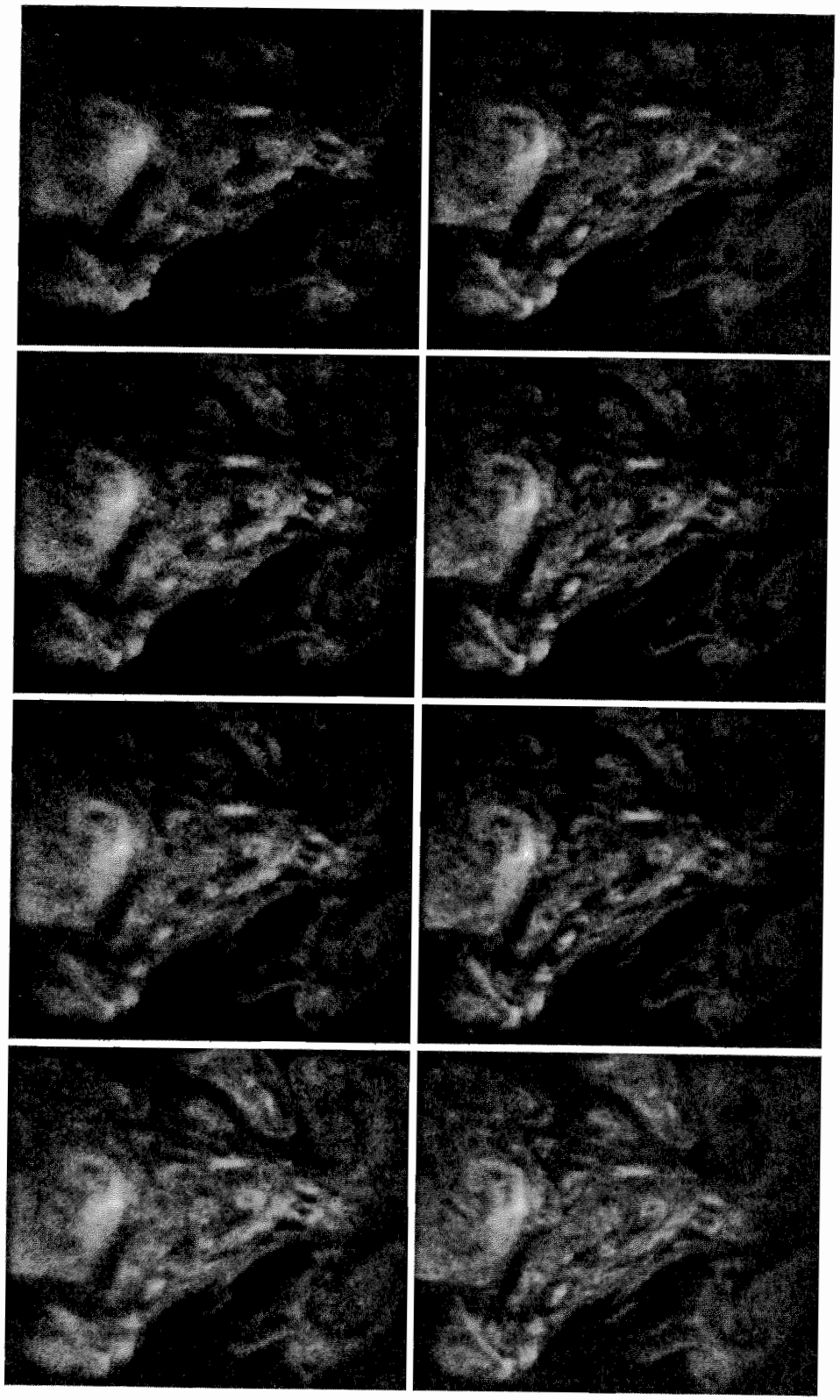

FIGURE 12. For caption see facing page.

FIGURE 13. A qualitative representation of the interface propagation in two images at slightly different times. The numbers on top correspond to the positions in the image sequence.

two successive images is comparable with the Batchelor scale. Figure 12 shows a sequence of images acquired in the axisymmetric jet.

By marking the position of the interface in two successive images, one can get an appreciation of the motion of the interface; this information is qualitative because one does not know where precisely a piece of the interface in one image ends up in the other. Figure 13 gives the positions of the interface in two images in a temporal sequence. The interface moves at different speeds at different positions, the speed being generally larger towards the front of the flow.

4. Scalar 'dissipation'

A quantity of practical interest, for example in the context of turbulent mixing of reactants involving fast chemistry, is the dissipation of passive scalar fluctuations $\chi = 2\Gamma(\partial\theta/\partial x_i)^2$, where x_i represent spatial coordinates and θ is a passive scalar (e.g. concentration c of a contaminant or temperature T), and Γ the corresponding molecular diffusivity; summation is implied on the index i. This dissipation is analogous to the dissipation of turbulent kinetic energy, ϵ, but different from it because it does not involve cross-terms and contains only three positive definite terms. All of them can in principal be obtained by the techniques used here. Since the resolution here is about three Kolmogorov scales, we obtain the quantity χ^*, where

$$\chi^* = [(\Delta c)/\Delta x_i]^2, \tag{4.1}$$

the difference concentration Δc being obtained with resolution of the order of 3η. For convenience, we have omitted the constant factor 2Γ in (4.1), and shall refer below to χ^* as the 'dissipation' rate. Figure 14 (*a–d*) shows for the jet the three components of χ^* and their sum obtained from a single frame of a jet image sequence such as that shown in figure 5. As expected, the 'dissipation' field is highly intermittent and the three components, while alike in the overall sense, have some differences. For example, χ_z^* appears to be less intermittent than the other two components, consistent with the single point measurements of Sreenivasan *et al.* (1977).

Using the temporal sequence of images, one can construct the χ^* field at different

FIGURE 12. A temporal evolution of the concentration of scalar-marked regions in an axisymmetric jet in an axial plane. The interframe time, 10^{-4} s, is comparable with the Batchelor timescale in the flow.

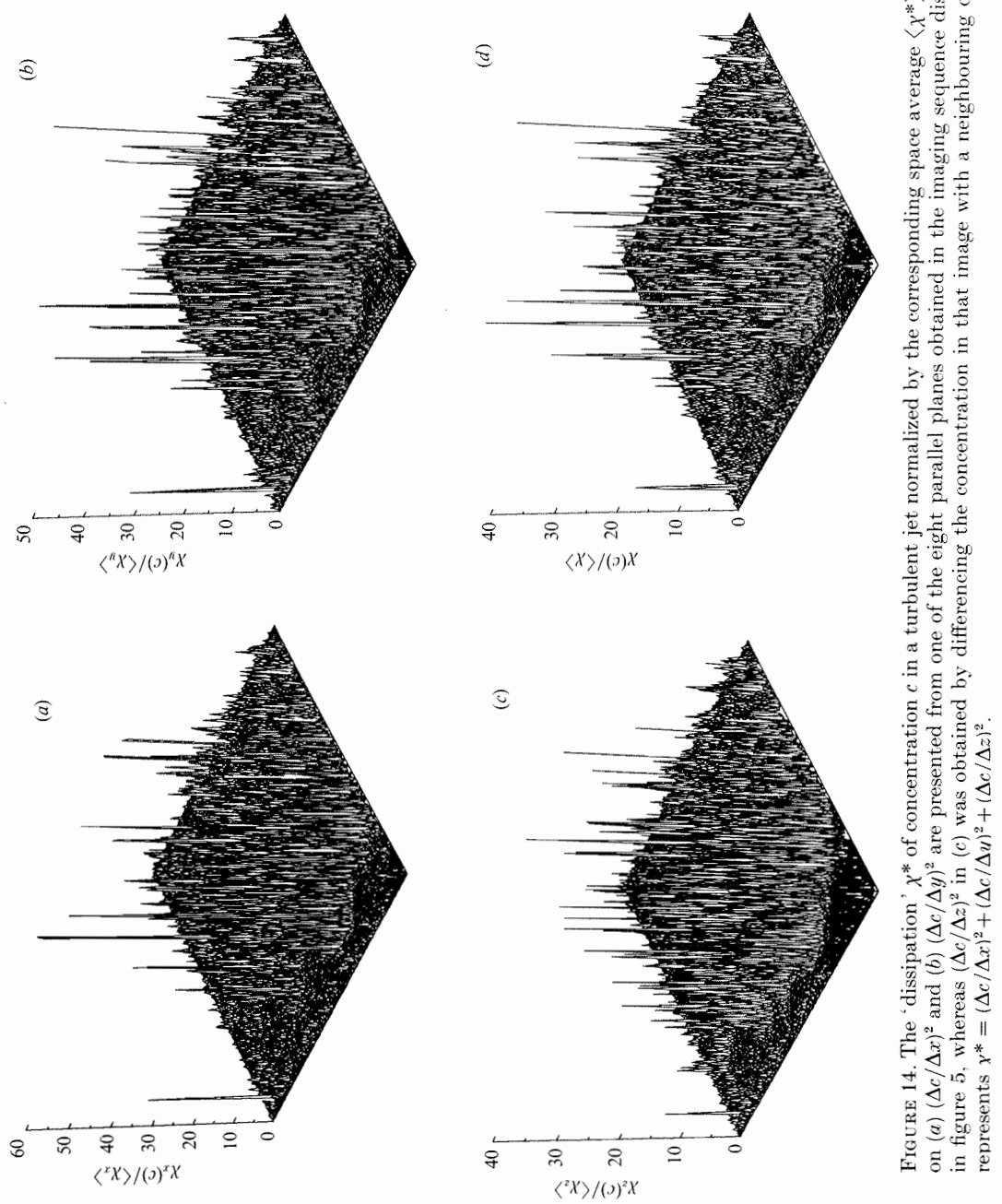

FIGURE 14. The 'dissipation' χ^* of concentration c in a turbulent jet normalized by the corresponding space average $\langle\chi^*\rangle$. Data on (*a*) $(\Delta c/\Delta x)^2$ and (*b*) $(\Delta c/\Delta y)^2$ are presented from one of the eight parallel planes obtained in the imaging sequence displayed in figure 5, whereas $(\Delta c/\Delta z)^2$ in (*c*) was obtained by differencing the concentration in that image with a neighbouring one; (*d*) represents $\chi^* = (\Delta c/\Delta x)^2 + (\Delta c/\Delta y)^2 + (\Delta c/\Delta z)^2$.

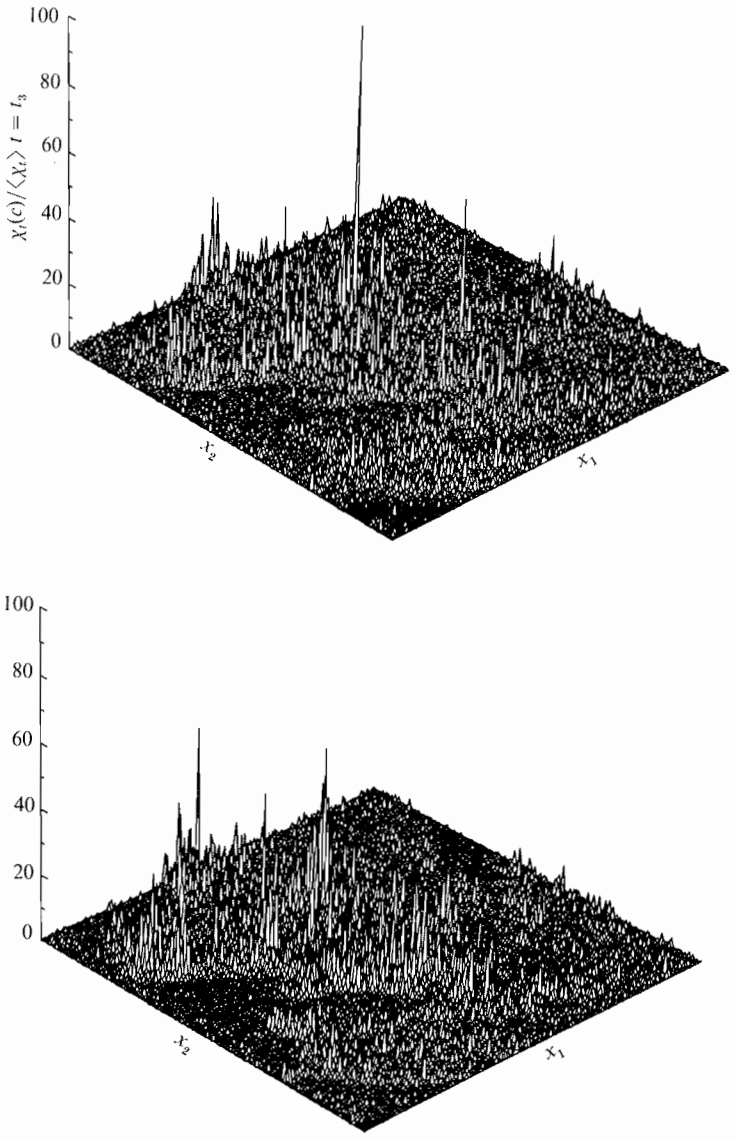

FIGURE 15. The 'dissipation' field at two successive instants of time which are 100 μs apart. Notice that the dissipation field has changed significantly in that time. It is evident that these changes cannot be attributed to advection by the mean motion because it is negligibly small. This behaviour is therefore attributed to temporal intermittency.

times in the same region of the flow. Two typical cases are shown in figure 15. The time interval between them is 10^{-4} s. During this interval, there is negligible motion – at any rate no more than about a pixel's equivalent. In view of this, it is interesting that large changes in the 'dissipation' field are observed at some locations in the images. We tentatively attribute this to temporal intermittency whose direct observation does not seem to have been made before.

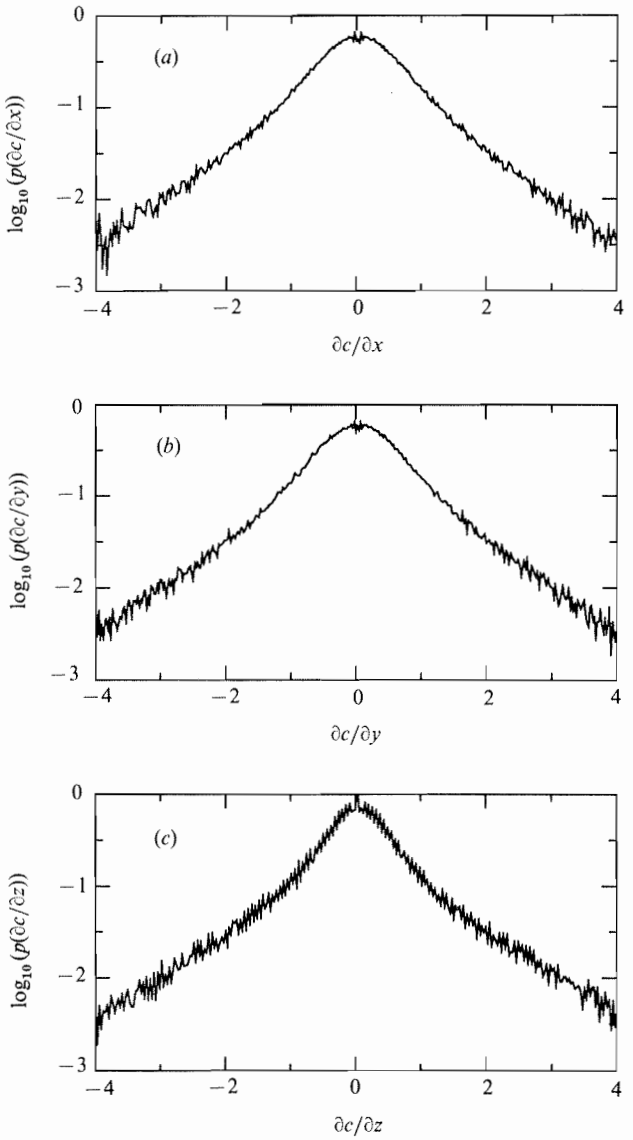

FIGURE 16. The normalized probability densities of the quantities $(\Delta c/\Delta x)$, $(\Delta c/\Delta y)$ and $(\Delta c/\Delta z)$. The abscissae are normalized by the respective root-mean-square values, and the ordinates are normalized correspondingly.

4.1. *Probability densities and moments*

For clarity in the following discussion, we reiterate that we have in each sequence all three components of χ^* in seven parallel planes of the flow. Ten such sequences were considered for each flow. We have found that the space averages of the components of χ^* are not equal in general even if the averaging domain is restricted to the interior regions of the flow. This is in contradiction to broad expectations of local isotropy. To assess the anisotropy in a gross sense, we have calculated the ratios χ_x^*/χ_z^* and χ_y^*/χ_z^* from a total of 75 image pairs. (Subscripts denote the directions of derivatives.) Averaging was performed over the entire extent of the images to avoid arbitrariness.

These ratios are 0.53 ± 0.18 and 0.71 ± 0.22, similar to the earlier findings from point measurements of Sreenivasan *et al.* (1977).

The normalized probability densities of the concentration gradients are given in figure 16 (*a–c*). These are averages taken over one sequence of images. There are some differences among the three gradients. We again call attention to exponential tails. The part of the probability density near zero concentration gradients is generally affected by the noise outside the scalar-marked regions, and possibly also the interface itself. If the averaging is restricted completely to regions interior to the interface, a larger segment of the curve can be represented by exponentials; also, the peak near zero concentration gets suppressed somewhat and becomes more rounded.

The skewness of the gradients, computed from the spatial averages over 70 image pairs, is close to zero even though it fluctuates from one image to the other rather strongly. Noting that the averaging is performed over the entire extent of the images in each case, the zero values for the skewness of $\Delta c/\Delta y$ and $\Delta c/\Delta z$ reflect the obvious symmetry in the flows. The similar behaviour shared by $\Delta c/\Delta x$ suggests that asymmetries in the x-direction are also not too large. The flatness factor for all three gradients, computed similarly, is about 10 for jets and about 30 for wakes; in general, wakes display larger intermittency.

4.2. *Joint statistics of the concentration and its 'dissipation'*

In figure 14 (*a–d*), we showed typical spatial distributions of χ_x^*, χ_y^*, χ_z^* and χ^*. In figure 17 (*a–d*) we show for the same case the products $c\chi_x^*$, $c\chi_y^*$, $c\chi_z^*$ and $c\chi^*$. (Note: c is not the concentration fluctuation, but the local concentration above zero in arbitrary units.) It is clear that the pictures are even more peaked and intermittent than the 'dissipation' itself, and values two orders of magnitude larger than the product of the means are not unlikely.

A quantity of interest in reacting flows is the joint probability density of the concentration and its dissipation; similar interest surrounds the conditional densities of the scalar and its three gradients. Figure 18 shows the joint densities of c and $\Delta c/\Delta x_i$, and of c and χ^*. Because the scalar dissipation possesses a sharp probability density with long tails, it is difficult to extract quantitative data from figure 18. For this reason, we have provided in figure 19 the iso-probability contours for c and $(\Delta c/\Delta z)$ and c and χ^*. The contours involving the other two gradients of c are not very different.

4.3. *Multifractal properties of the dissipation field*

A fundamental aspect of the dissipation field is its spatial and temporal intermittency. It is clear that such highly intermittent processes cannot be described efficiently by conventional moment methods which are good for Central Limit-type processes; in particular, the mean and the variance of a Gaussian process describe it completely. For processes which are close to Gaussian, it can be expected that a few low-order moments contain most of the information. On the other hand, for processes of the type shown in figure 14, it is clear that the first few moments give very little clue to their nature.

It has been recognized (Mandelbrot 1974; Frisch & Parisi 1985; Halsey *et al.* 1986) that intermittent measures arising in nonlinear systems lend themselves to be characterized by what are called multifractals in the present parlance of dynamical systems. For a historical account of the subject of multifractals see the above references and Meneveau & Sreenivasan (1987). One way of building multifractals is to proceed from one scale (to be called the parent scale) to the next smaller ones (the

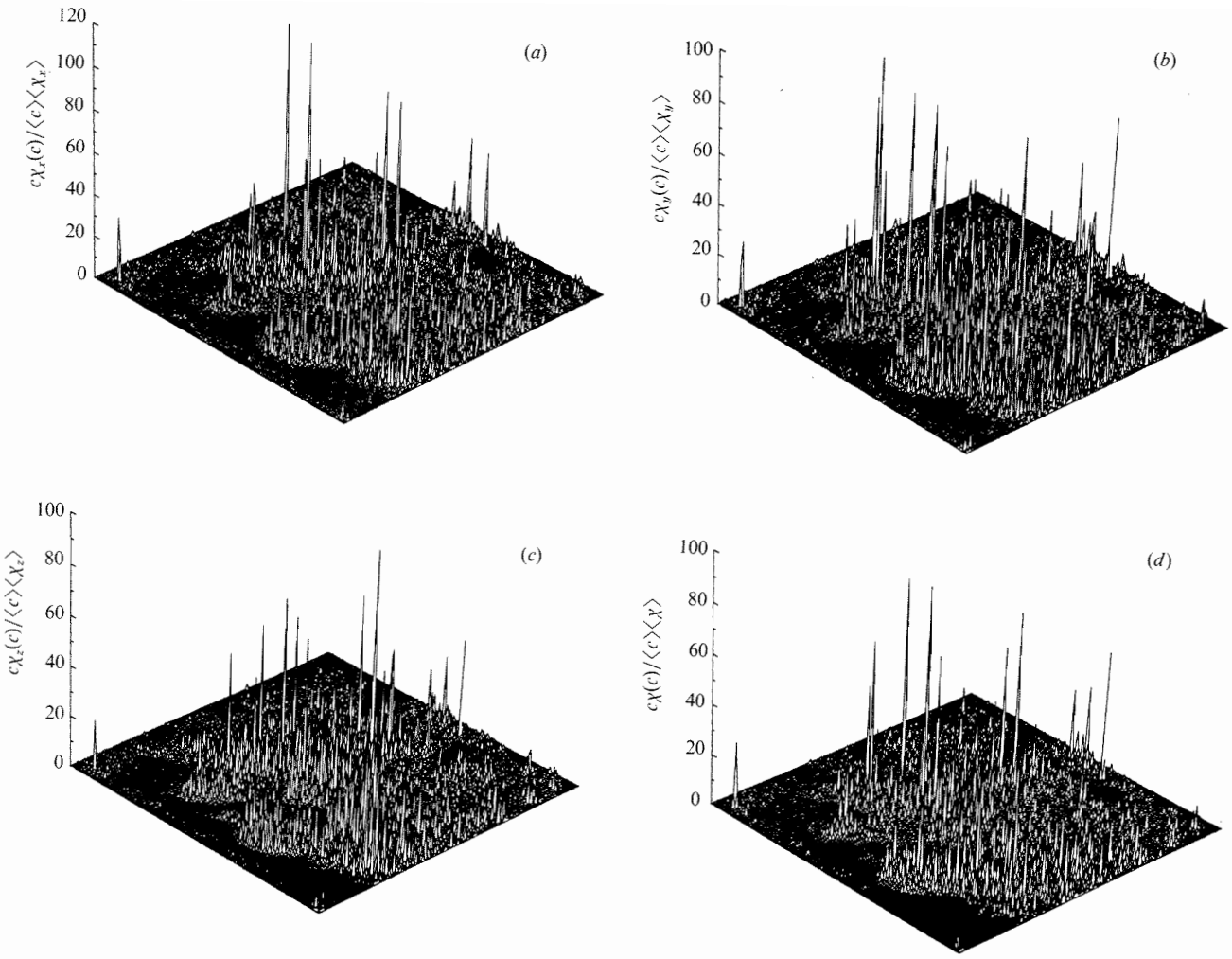

FIGURE 17. The product of the 'dissipation' χ^* of concentration c in a turbulent jet normalized by the corresponding product of the averages $\langle c\rangle\langle\chi^*\rangle$. The squares of the gradients in figure 14 were multiplied by the concentration field to obtain these figures.

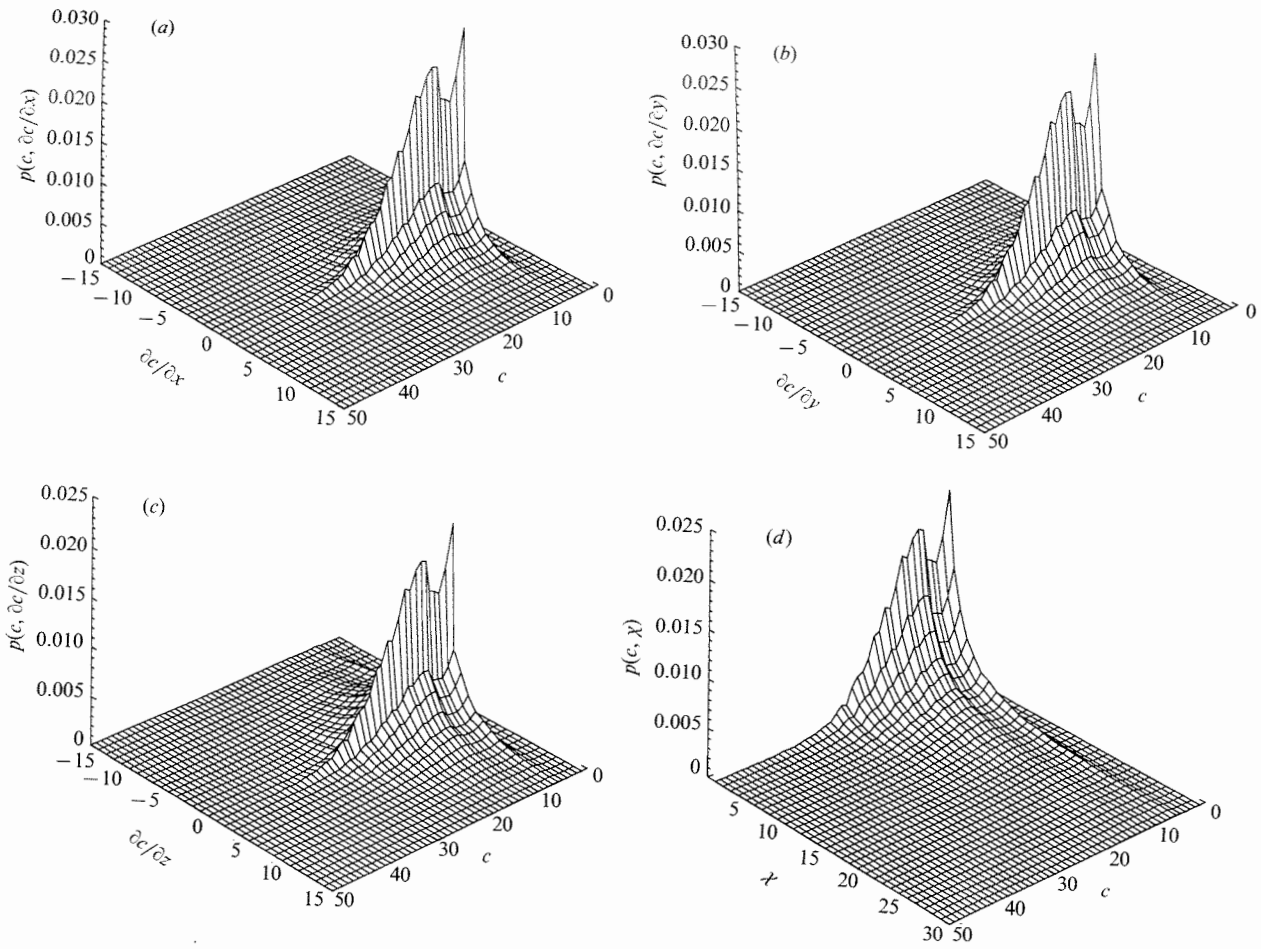

FIGURE 18. (*a*), (*b*) and (*c*) Joint probability densities of c and its three spatial derivatives in directions x, y and z respectively, and (*d*) that between c and χ^*. The ordinate in each case is normalized as in figure 8.

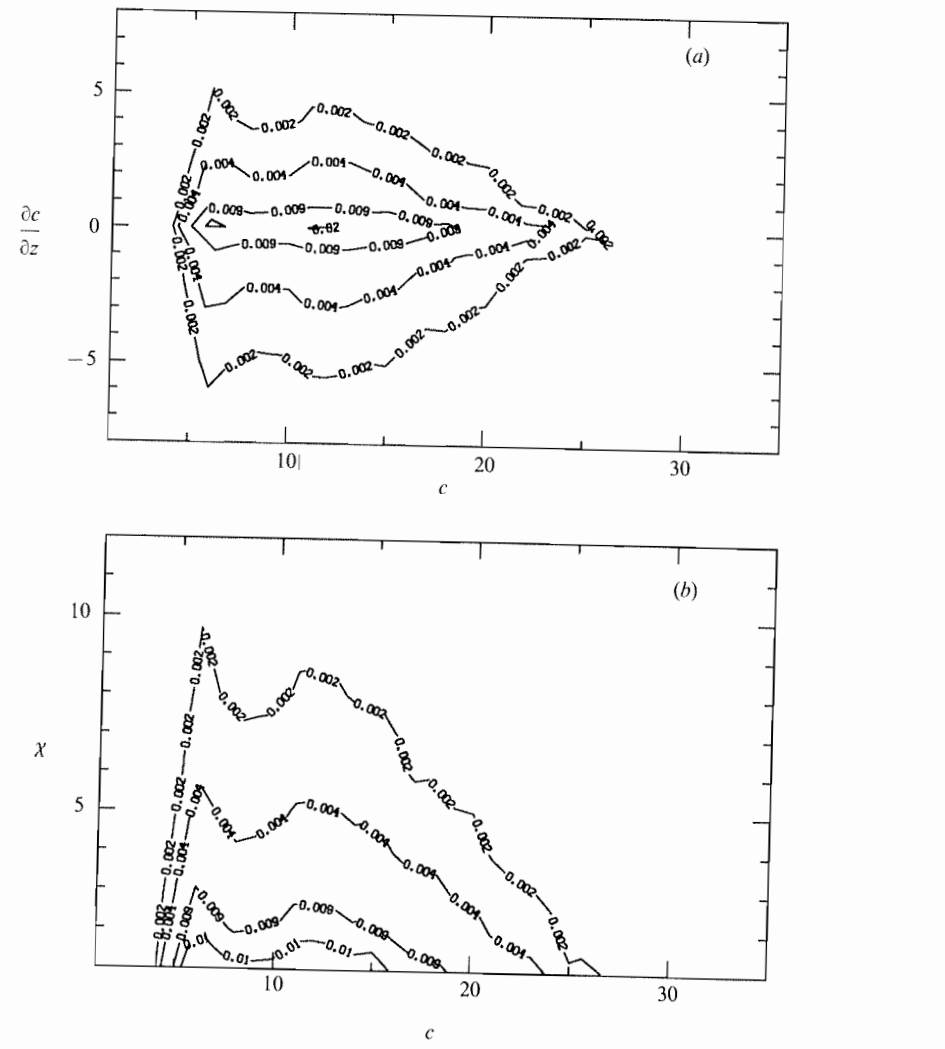

FIGURE 19. Iso-probability contours for the joint densities. They are similar for all three gradients, but that involving the gradient $\Delta c/\Delta z$ is shown – partly as a representative and partly because it is the hardest to measure.

offspring) in such a way that the measure (roughly, the flux of scalar 'dissipation') contained by the parent scale is unequally divided among its offspring. When such a procedure is repeated over many steps, it is clear that the measure on each succeedingly higher generation offspring will become more and more uneven. If the basic rule determining the nature of the unequal division from a parent scale to its offspring is independent of the generation level, one expects to see certain scale similar properties. Since the measure on an arbitrarily chosen offspring at any given generation level is determined by the product of the multipliers (that is to say, numbers characterizing the unequal division of the measure) of all its forefathers, a multifractal is associated with a multiplicative process. Under certain restrictive circumstances, the underlying multiplicative process can be identified uniquely by studying the scaling structure of the multifractal; this, however, is an exception rather than the rule (Chhabra, Jensen & Sreenivasan 1989).

Because the measure associated with an offspring at any level is the product of the multipliers of all its forefathers, it is clear that the scaling will only be local; there is therefore the expectation that many, in fact infinitely many, scaling indices are necessary to describe multifractals. The purpose of analysis is to quantify these various scaling indices and unravel some of their properties. A practical way of doing it is to divide the domain in which the 'dissipation' resides into boxes of a certain size, and to write that the total amount of 'dissipation' on each of these boxes follows power laws of the following type:

$$\boldsymbol{X}_r \sim r^{\alpha(\boldsymbol{x})}, \tag{4.2}$$

where $\boldsymbol{X}_r$ is the integral of χ^* over a box of size r, and $\boldsymbol{x}$ is the position of the (centre of the) box in the space in which the multifractal is embedded. The rationale for writing (4.2) is merely that it generalizes our perception in Euclidean geometry, for which the index α would be equal to the dimension of the embedding space d (that is, unity in one-dimensional space, 2 in two-dimensional space and so on). For fractal distributions, α can have non-integer values. If the scaling were global, as in the case of unifractals (which is what one understands usually by the term fractal), one would expect α to be independent of position in the embedding space. A characteristic of multifractals is that α depends on $\boldsymbol{x}$. In general, α is bounded on both sides by an $\alpha_{\min}$ and an $\alpha_{\max}$.

A significance of the index α (called variously as the Hölder exponent or the crowding index) becomes obvious if we rewrite from (4.2) an expression for the intensity of dissipation χ_r in a box of size r. Since this is merely the total amount of dissipation $\boldsymbol{X}_r$ in a box of size r divided by the 'volume' of the box, we get for a d-dimensional space

$$\chi_r \sim r^{\alpha(\boldsymbol{x})-d}. \tag{4.3}$$

According to (4.3), whenever $\alpha(\boldsymbol{x}) < d$, χ_r increases indefinitely as the box size shrinks, and represents spikes (or, singular regions) in the distribution of χ_r; smaller values of α represent larger spikes. On the other hand, α-values greater than d represent smooth (or regular) distributions, and hence α can be thought of an index which characterizes 'singularities' of different strengths. This interpretation has been taken to its logical conclusion in the case of energy dissipation (Sreenivasan & Meneveau 1988).

Now, corresponding to each α, or each iso-α set, one can identify a fractal dimension $f(\alpha)$. That is, the number $N_r(\alpha)$ of boxes of size r covering the iso-α set varies as

$$N_r(\alpha) \sim r^{-f(\alpha)}. \tag{4.4}$$

Recalling the similar expression for the number of boxes in the case of fractals (see §3), we see that $f(\alpha)$ has the meaning of the fractal dimension of the iso-α set. In this picture, local singularities of different strengths α are distributed on interwoven sets of varying dimensionality $f(\alpha)$. A curve of f *vs.* α is therefore a means of disentangling fractal sets which are interwoven together to give the complicated multifractal under consideration.

In a different framework, Hentschel & Procaccia (1983) showed that moments of order q obey power laws and involve the so-called generalized dimensions D_q. In the present context, the set of generalized dimensions D_q is defined by dividing an appropriately chosen 'dissipation' region into smaller square regions of size r, and by identifying power-laws (Hentschel & Procaccia 1983; Halsey *et al.* 1986; Meneveau & Sreenivasan 1987) of the type

$$\sum (\boldsymbol{X}_r/\boldsymbol{X}_L)^q \sim r^{(q-1)D_q}, \tag{4.5}$$

where $\boldsymbol{X}_L$ is the total dissipation, and the sum is taken over all squares of size r contained in the domain. The meaning of raising the measure $\boldsymbol{X}_r$ to a power q is that, if q is positive and large, only the large-intensity regions will be picked by the summation in (4.4) while least intense regions correspond to D_q with large negative q. According to (4.5), if log–log plots of $[\Sigma(\boldsymbol{X}_r/\boldsymbol{X}_L)^q]^{1/(q-1)}$ *vs.* r present linear regions for r within a certain scaling range, then the slopes correspond to D_q. From the D_q curves, the $f(\alpha)$-curves can be computed using the Legendre transforms (Halsey *et al.* 1986; Meneveau & Sreenivasan 1987)

$$\alpha = \mathrm{d}/\mathrm{d}q[(q-1)D_q], \quad f(\alpha) = q\alpha-(q-1)D_q. \tag{4.6a, b}$$

In some form, these ideas have been discussed in the context of turbulence by Mandelbrot (1974), Benzi *et al.* (1984) and Frisch & Parisi (1985). The first measurements were made by Meneveau & Sreenivasan (1987) for the energy dissipation and by Prasad *et al.* (1988) for the scalar 'dissipation' field. Meneveau & Sreenivasan (1987) have measured the D_q *vs.* q curve and f *vs.* α curves for one-dimensional sections of the dissipation of turbulent kinetic energy, and shown them to be universal features of fully developed turbulence. Prasad *et al.* (1988) obtained two components of the scalar 'dissipation' from two-dimensional LIF images. Here, since we are capable of measuring all three components of χ^*, some useful results on the nature of differences among them can be obtained. Our purpose here to measure the D_q *vs.* q and $f(\alpha)$ *vs.* α curves, and examine the multifractal properties of χ^* as well as of each of its three components.

Several methods can be used for the computation of the $f(\alpha)$-curve. Following the lead of Halsey *et al.* (1986) in dynamical systems, Meneveau & Sreenivasan and Prasad *et al.* used a procedure that requires the computation of the generalized dimensions first, and the use of Legendre transforms (4.6). Direct methods of computing the $f(\alpha)$-curve have been applied to turbulence data (Meneveau & Sreenivasan 1989; Chhabra *et al.* 1989). We have resorted to the intermediary of the generalized dimensions. As explained above, this requires the computations of the slopes in the log–log plots of $[\Sigma(\boldsymbol{X}_r/\boldsymbol{X}_L)^q]^{1/(q-1)}$ *vs.* r. This is repeated for 12 different values of r ranging from 1 pixel, corresponding roughly to $r = 3\eta$, up to $r = 150$ pixels.

Typical log–log plots of $[\Sigma(\boldsymbol{X}_r/\boldsymbol{X}_L)^q]^{1/(q-1)}$ *vs.* r are shown in figure 20 for representative q values. A scaling range can be observed from $r \sim 1$ pixel to $r \sim 80$ pixels. The slopes of these straight lines give D_q. From the average D_q values taken over many realizations and the use of the Legendre transforms (4.6), the $f(\alpha)$ *vs.* α curve was computed.

It is now possible to compare the $f(\alpha)$ measured using each of the different components of the dissipation field. Similar comparisons have been reported earlier (Prasad *et al.* 1988), but all three components of χ^* were not measured simultaneously as they are in this investigation. Figure 21 shows the $f(\alpha)$-curve computed for the jet using each of the three components independently as well as for the total 'dissipation' field. The $f(\alpha)$ values for all of them agree well within experimental uncertainties. This is an important result in that it establishes that the multifractal properties of the 'dissipation' can be obtained by using only one of its three components.

We have also processed the wake data similarly, and found that they agree well with the jet data. This suggests that the $f(\alpha)$-curve is a universal property of the 'dissipation' field of the scalar, confirming a similar conclusion of Meneveau & Sreenivasan (1987) for the energy dissipation field.

(We should make an important point here for experts on multifractals. In two-

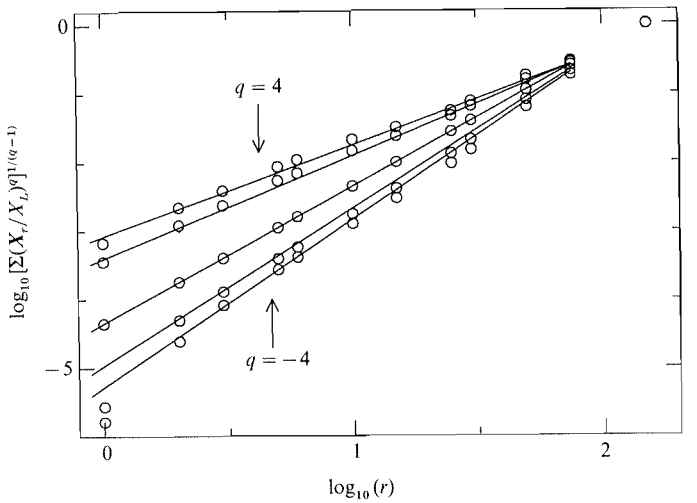

FIGURE 20. Typical log–log plots of $[\Sigma(\boldsymbol{X}_r/\boldsymbol{X}_L)^q]^{1/(q-1)}$ *vs.* r from the dissipation field of the wake for five different values of q: $-4, -2, 0, 2, 4$. Power law regions are seen for each q, extending from $r \sim 1$ pixel to $r \sim 80$ pixels.

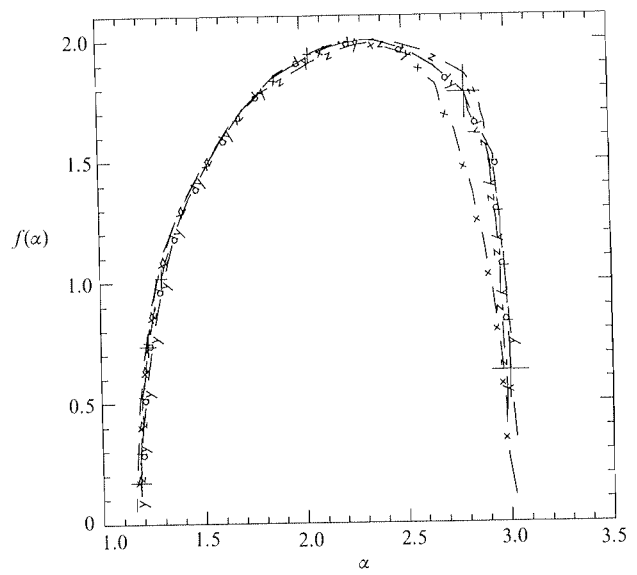

FIGURE 21. The $f(\alpha)$-curves calculated using each of the different components of χ^*. The -x- curve represents the x-component, the -y- curve the y-component, the -z- curve the z-component and the -d- curve the total 'dissipation' field.

dimensional images, Prasad *et al.* (1988) selectively chose regions of scalar fluctuations which were away from the interface. That is, their $f(\alpha)$-curve was appropriate to the dynamics of the flow interior. While this choice is always possible in one-dimensional sections on the axis and carefully chosen parts of two-dimensional images, it is essentially impossible in three dimensions; for, however small a domain one chooses (as long as it is bigger than the inner cut-off scale), the interface intersects that domain at some place or another. Thus, it is in principle impossible to find the $f(\alpha)$-curve only for the interior region, and the entire image including the

interface should be considered *in toto*. This makes no difference to small α-values which correspond to high-intensity regions of the dissipation found only in the interior, but this is of some consequence to the larger values of α. Since there is always a jump (even though not a large one) of concentration across the interface, inclusion of the interface will always produce peaks of some magnitude in χ^* in any box one chooses. Thus, there will nowhere be regions where large α values can be found; technically, therefore, some values of α would be absent. The $f(\alpha)$-curve should therefore be very similar to that of the interior for all values of α below a certain value, but must show a precipitous drop at some larger value. Equivalently, the D_q curve for q lower than a certain value will either flatten or increase much less rapidly. We tentatively propose that this sudden drop can be thought of in a rough sense as corresponding to a (phase) transition from bulk-dominated properties to surface-dominated properties.)

4.4. *Resolution effects*

An important question concerns scalar fluctuations on scales below the Kolmogorov scale which remain unresolved in present experiments. For example, what effect does this have on the statistical properties including multifractal spectra? This has been considered briefly in Prasad & Sreenivasan (1990) by making single point measurements of dye concentration fluctuations in jets and wakes by optical methods. The spatial resolution was of the order of 4 μm (comparable with the Batchelor scale) and the frequency response (of at least up to 320000 Hz) resolved the corresponding timescale. For details of how such fine resolutions were obtained, the reader should consult the reference cited above. We verified that conventional spectral data showed the expected scaling in the regimes between η and η_b and between η and L.

Multifractal spectra were obtained separately for the two scaling regimes. Taylor's hypothesis was used, but its usefulness in this specific context was established (however, with some important qualifications) in Prasad, Meneveau & Sreenivasan (1990). When the additive law (§3.4) was applied, the multifractal spectrum for the scale range between L and η agreed well with the present data. The conclusion is that the scaling properties in the two regimes are independent of each other. Further, we also computed from these finely resolved data the p.d.f.s for the concentration fluctuations and its gradients. The finer-resolution data detected outer intermittency regions that were not registered in measurements with coarser resolution, and displayed a much sharper peak corresponding to the zero concentration of the outer tank fluid. Other parts of the p.d.f. distributions are essentially the same.

5. Summary of conclusions

We have measured, with spatial resolution of the order of the Kolmogorov scale, the three-dimensional field of a passive scalar in fully turbulent flows at moderate Reynolds numbers. The technique consists of the quantitative mapping, effectively instantaneously, of the concentration field in several parallel planes. This is made possible by combining the unique capabilities of the framing camera with a relatively large CCD array. The measurements allow us to examine several issues concerning the three-dimensional structure of the passive scalar field. First, some aspects of the scalar interface have been studied. We showed that the scalar-marked regions do not generally detach themselves from the main body. We then devised a simple scheme for correlating the interface shape from one parallel plane to another. Its

application showed that, in spite of the large structure, the randomness associated with small-scale convolutions of the interface are strong enough that any two intersections of it by parallel planes are essentially uncorrelated even if the separation distances are of the order of a few Kolmogorov scales. The fractal dimension of the interface was determined directly by box counting in three dimensions, and the value of 2.35 ± 0.04 is shown to be in excellent agreement with that previously inferred from two-dimensional sections. This justifies the use of the method of intersections. Finally, we obtained a time sequence of two-dimensional images resolving motions associated with the Batchelor scale; this enables us to detect temporal intermittency in turbulent flows, and qualitatively the propagation speeds of the scalar interface.

The second contribution involves the joint statistics of the scalar field and the quantity χ^* which is the appropriate approximation (due to finite resolution effects) to the scalar dissipation field in the inertial–convective range of scales. Here, we showed that the variances (with averaging performed over space) of the three components of χ^* are substantially different in magnitude, but their non-dimensional probability functions are not very different – at least to the extent that the third- and fourth-order moments are concerned. Several measures of the joint probability density between the concentration c and its 'dissipation', and that between c and its spatial derivatives have been measured.

The third aspect relates to the *multifractal scaling properties* of the spatial intermittency of χ^*; since all three components of χ^* have been obtained effectively simultaneously, inferences concerning the scaling properties of the individual components and their sum have been possible. The usefulness of the multifractal approach for describing highly intermittent distributions of χ^* and its components is explored by measuring the so-called singularity spectrum (or the $f(\alpha)$-curve) which quantifies the spatial distribution of various strengths of χ^*. We have shown that a single component can serve as an excellent surrogate for the total dissipation.

We have also established the quality of the data by making, where possible, comparisons with previous measurements. Although the resolution in the present measurements is on the order of three Kolmogorov scales, it has been argued that the scaling properties in the appropriate scaling range are correct.

Finally, we note that the analysis of these three-dimensional data is by no means complete at this stage, and we are in the process of extracting more physical features of the scalar field.

K.R.S. thanks Professor Mitchell Feigenbaum for his hospitality at Rockefeller University where part of this writing was done. We thank Marshall Long and Brandon Yip for some helpful comments concerning the instrumentation, and Robert Bilger and Charles Meneveau for their comments on the manuscript. The research was made possible by the financial assistance from a DARPA (URI) grant and an instrumentation grant from AFOSR.

REFERENCES

Agüí, J. C. & Hesselink, L. 1988 *J. Fluid Mech.* **191**, 19.

Batchelor, G. K. 1959 *J. Fluid Mech.* **5**, 113.

Benzi, R., Paladin, G., Parisi, G. & Vulpiani, A. 1984 *J. Phys.* A **17**, 3521.

Bilger, R. W., Antonia, R. A. & Sreenivasan, K. R. 1978 *Phys. Fluids* **19**, 1471.

Castaing, B., Gunaratne, G., Heslot, F., Kadanoff, L., Libchaber, A., Thomae, S., Wu, X.-P., Zaleski, S. & Zanetti, G. 1989 *J. Fluid Mech.* **204**, 1.

CHATWIN, P. C. & SULLIVAN, P. J. 1989 *Phys. Fluids* A **1**, 761.

CHHABRA, A., JENSEN, R. & SREENIVASAN, K. R. 1989 *Phys. Rev.* A **40**, 4593.

CHHABRA, A., MENEVEAU, C., JENSEN, R. V. & SREENIVASAN, K. R. 1989 *Phys. Rev.* A **40**, 5284.

CORRSIN, S. & KISTLER, A. L. 1955 *NACA Rep.* 1244.

DAHM, W. & BUCH, K. 1989 Poster paper (forum 13) in the *Seventh Turbulent Shear Flow Conference, Stanford.*

DIMOTAKIS, P. E., LYE, R. C. M. & PAPANTONIOU, D. A. 1983 *Phys. Fluids* **28**, 3185.

EVERSON, R., SIROVICH, L. & SREENIVASAN, K. R. 1990 *Phys. Lett.* A (to appear).

FEIGENBAUM, M. J., JENSEN, M. H. & PROCACCIA, I. 1986 *Phys. Rev. Lett.* **57**, 1507.

FRISCH, U. & PARISI, G. 1985 In *Turbulence and Predictability in Geophysical Fluid Dynamics and Climate Dynamics* (ed. M. Ghil, R. Benzi & G. Parisi), p. 84. North-Holland.

GOULDIN, F. C. 1988 *AIAA J.* **26**, 1405.

HALSEY, T. C., JENSEN, M. H., KADANOFF, L. P., PROCACCIA, I. & SHRAIMAN, B. I. 1986 *Phys. Rev.* A **33**, 1141.

HENTSCHEL, H. G. E. & PROCACCIA, I. 1983 *Physica* **8D**, 435.

KLEBANOFF, P. S. 1955 *NACA Rep.* 1247.

KOLMOGOROV, A. N. 1962 *J. Fluid Mech.* **13**, 82.

KYCHAKOFF, G., PAUL, P. H., CRUYNINGEN, I. VAN & HANSON, R. K. 1987 *Appl. Optics* **26**, 2498.

LYNCH, M. K., MILLER, P., LEWIS, C. & NOSENCHUCK, D. M. 1985 *Bull. Am. Phys. Soc.* **30**, 1751.

MANDELBROT, B. B. 1974 *J. Fluid Mech.* **62**, 331.

MANDELBROT, B. B. 1982 *The Fractal Geometry of Nature.* W. H. Freeman.

MARSTRAND, J. M. 1954 *Lond. Math. Soc.* **3**, 257.

MENEVEAU, C. & SREENIVASAN, K. R. 1987 In *The Physics of Chaos and Systems far from Equilibrium* (ed. Minh-Duong Van), p. 49. *Nuclear Phys.* B (*Proc. Suppl.*) **2**. North-Holland.

MENEVEAU, C. & SREENIVASAN, K. R. 1989 *Phys. Lett.* A **137**, 103.

POPE, S. B. 1988 *Intl J. Engng Sci.* **26**, 445.

PRASAD, R. R. 1989 In *Forum on Chaotic Dynamics in Fluid Mechanics, La Jolla.* ASME.

PRASAD, R. R., MENEVEAU, C. & SREENIVASAN, K. R. 1988 *Phys. Rev. Lett.* **61**, 74.

PRASAD, R. R., MENEVEAU, C. & SREENIVASAN, K. R. 1990 (in preparation).

PRASAD, R. R. & SREENIVASAN, K. R. 1989 *Expts in Fluids* **7**, 259.

PRASAD, R. R. & SREENIVASAN, K. R. 1990 *Phys. Fluids* A (to appear).

SREENIVASAN, K. R. 1985 *J. Fluid Mech.* **151**, 81.

SREENIVASAN, K. R., ANTONIA, R. A. & DANH, H. Q. 1977 *Phys. Fluids* **20**, 1238.

SREENIVASAN, K. R. & MENEVEAU, C. 1986 *J. Fluid Mech.* **173**, 357.

SREENIVASAN, K. R. & MENEVEAU, C. 1988 *Phys. Rev.* A **38**, 6287.

SREENIVASAN, K. R. & PRASAD, R. R. 1989 *Physica D* **38**, 322.

SREENIVASAN, K. R., RAMSHANKAR, R. & MENEVEAU, C. 1989 *Proc. R. Soc. Lond.* A **421**, 79.

TOWNSEND, A. A. 1948 *Austral. J. Sci. Res.* **23A**, 451.

WARE, B. R., CYR, D., GORTI, S. & LANNI, F. 1983 In *Measurement of Suspended Particles by Quasi-Elastic Light Scattering* (ed. B. E. Dahneke), p. 255. Wiley.

YIP, B. 1988 Ph.D. thesis, Yale University.

YIP, B., FOURGETTE, D. C. & LONG, M. B. 1986 *Appl. Optics* **25**, 3919.

YIP, B., LAM, J. K., WINTER, M. & LONG, M. B. 1987 *Science* **235**, 1209.